AGU PUBLICATIONS

JGR

Journal of Geophysical Research: Atmospheres

RESEARCH ARTICLE

10.1002/2016JD025456

Key Points:
- Satellite precipitation evaluation
- Intercomparison of multisatellite precipitation products over China

Correspondence to:
Y. Zhou,
yangzhou@nju.edu.cn

Citation:
Huang, A., Y. Zhao, Y. Zhou, B. Yang, L. Zhang, X. Dong, D. Fang, and Y. Wu (2016), Evaluation of multisatellite precipitation products by use of ground-based data over China, *J. Geophys. Res. Atmos.*, *121*, 10,654–10,675, doi:10.1002/2016JD025456.

Received 1 JUN 2016
Accepted 26 AUG 2016
Accepted article online 1 SEP 2016
Published online 28 SEP 2016

Evaluation of multisatellite precipitation products by use of ground-based data over China

Anning Huang[1], Yong Zhao[2], Yang Zhou[1], Ben Yang[1], Lujun Zhang[1], Xinning Dong[3], Dexian Fang[4], and Yang Wu[1]

[1]CMA-NJU Joint Laboratory for Climate Prediction Studies, School of Atmospheric Sciences, Nanjing University, Nanjing, China, [2]School of Atmospheric Sciences, Chengdu University of Information Technology, Chengdu, China, [3]Chongqing Climate Center, Chongqing, China, [4]Chongqing Institute of Meteorology and Science, Chongqing, China

Abstract Five satellite precipitation products, including Climate Prediction Center Morphing Technique (CMORPH), Precipitation Estimation From Remotely Sensed Information Using Artificial Neural Network (PERSIANN), Tropical Rainfall Measuring Missing (TRMM) Multisatellite Precipitation Analysis (TMPA) version 7 products 3B41RTV7, 3B42RTV7, and 3B42V7, are systematically evaluated by comparing to the daily precipitation data collected from ~2400 gauge stations over China during January 2000 to December 2014. Satellite estimates generally capture the overall spatial-temporal variation of precipitation over China with relatively better ability in warm seasons than in cold seasons. Meanwhile, satellite precipitation estimates also tend to show better agreement with gauge observations over humid regions than over arid and alpine regions. Analysis of the systematic and random error components suggests that the uncertainties in both TRMM3B42RTV7 and TRMM3B42V7 precipitation estimates are significantly reduced over most parts of China compared to the other three satellite products. Among the five products, the research product TRMM3B42V7 with bias adjustments agrees the most with the gauge observation in terms of spatiotemporal variation, amplitude and pattern of variability, occurrence of rainy events, and probability distribution function of the precipitation amount for different rain rates over most parts of China; the near-real-time product TRMM3B42RTV7 with the application of improved retrieval algorithms and more satellite data performs the second best over most subregions of eastern China. The improvements of TRMM3B42RTV7 without bias adjustments over eastern China relative to CMORPH, PERSIANN, and TRMM3B41RTV7 are encouraging and favorable for the operational applications.

1. Introduction

Precipitation, which is closely correlated with the changes of the water phase among vapor, liquid, and solid, is a major component of the global water and energy cycle that significantly affects the Earth's climate system and is influenced by climate system variability and change in turn [*Javanmard et al.*, 2010]. Precipitation is also a fundamental physical process of the hydrological cycle and land-atmosphere interactions [*Dai and Deser*, 1999] and has significant impact on the land surface hydrological fluxes and states [*Fekete et al.*, 2004; *Gottschalck et al.*, 2005; *Tian et al.*, 2007]. High resolution precipitation observations are essential for studying the global hydrological cycle [*Faures et al.*, 1995; *Nykanen et al.*, 2001; *Wang et al.*, 2015], mitigating worldwide droughts and floods [*Hossain and Anagnostou*, 2004], simulating land surface hydrological processes [*Nijssen and Lettenmaier*, 2004], revealing the water resources state [*Hong et al.*, 2007a, 2007b; *Sorooshian et al.*, 2005], land data assimilation applications [*Gottschalck et al.*, 2005; *Tian et al.*, 2007], discovering the precipitation diurnal variations [*Dai et al.*, 2007; *Zhou et al.*, 2008], and numerical model validation [*Adler et al.*, 2003; *Sorooshian et al.*, 2002; *Gottschalck et al.*, 2005]. However, reliable and accurate estimation of precipitation on regional and global scales remains a big challenge due to its large variability in space and time [*Chen et al.*, 2013a].

The conventional precipitation measurements at point-based gauge stations provide relatively longer and accurate measurements of precipitation at the station locations [*Yatagai et al.*, 2009]; however, they are only available over limited land regions [*Higgins et al.*, 1996]. In addition, the quality of gauge-based precipitation network relies strongly upon the configuration and density of the stations [*Morrissey et al.*, 1995]. In areas of sparse gauge stations, such as desert and complex mountainous areas, gauge network cannot sufficiently provide reliable spatial representation of precipitation [*Gruber and Levizzani*, 2008; *Xue et al.*, 2013]. To solve this problem, remote sensing of radar/radiometer and microwave imaging from space are widely used to compensate the limitations of surface gauge observations [*Schulz et al*., 2009]. Currently, as a successor to Tropical Rainfall Measuring Mission (TRMM), the Global Precipitation Measurement (GPM) mission is expected to provide next generation of precipitation measurements from space with more reliable global precipitation products than current TRMM Multisatellite Precipitation Analysis (TMPA) [*Chen et al*., 2013a; *Hou et al*., 2014; *Liu*, 2016].

During the past several years, a number of satellite-derived near global precipitation products [*Ebert et al*., 2007] with spatial resolution of at least 0.25° and temporal resolution of at least 3 h were developed, including the Climate Prediction Center morphing technique (CMORPH) [*Joyce et al*., 2004], Precipitation Estimation from Remotely Sensed Information Using Artificial Neural Networks (PERSIANN) [*Hong et al*., 2005; *Sorooshian et al*., 2000], TRMM TMPA, the Naval Research Laboratory (NRL) satellite precipitation estimates [*Turk and Miller*, 2005; *Turk et al*., 2010], and the passive microwave (PM)-calibrated infrared (IR) algorithm (PMIR) [*Kidd et al*., 2003]. These products generally merge IR data from geostationary satellites [*Arkin and Meisner*, 1987; *Susskind et al*., 1997; *Xie and Arkin*, 1998] and PM data from low orbiter satellites [*Ferraro*, 1997; *Spencer*, 1993; *Wilheit et al*., 1991] through taking advantage of the frequent sampling of the IR and the superior quality of the PM data to improve spatial precipitation estimates [*Grimes and Diop*, 2003]. These satellite precipitation products are useful for many important applications, such as weather/climate monitoring, climate analysis, numerical model validation, and hydrological studies [*Janowiak et al*., 2005; *Yang and Smith*, 2006; *Harris et al*., 2007; *Collischonn et al*., 2008; *Kidd et al*., 2009; *Li et al*., 2012; *Liechti et al*., 2012]. They are especially valuable in developing countries or remote areas with sparse or bad quality conventional gauge-based data [*Hughes*, 2006; *Xue et al*., 2013]. Furthermore, the near-real-time availability of the satellite-derived precipitation products makes them suitable for modeling applications over the regions where water resources management is crucial and data gathering and quality assurance are cumbersome [*Stisen and Sandholt*, 2010].

Satellite precipitation products can provide quasi-global high-quality precipitation maps, but they are subject to biases and systematic errors caused by various factors like sampling frequency, nonuniform field of view of the sensors, and uncertainties in the retrieval algorithms [*Nair et al*., 2009]. It is therefore necessary to evaluate and intercompare these data sets before application [*Ebert et al*., 2007; *Chokngamwong and Chiu*, 2008; *Dinku et al*., 2007, 2008]. In addition, the evaluation is also favorable for the improvement of the retrieval algorithms [*Kidd et al*., 2012]. A number of efforts have recently been carried out to compare different satellite precipitation products with ground-based observation over South America [*Su et al*., 2008], North America [*Hong et al*., 2007c], East Asia [*Xie et al*., 2007], tropical Indian Ocean, the United States and Pacific Ocean [*Sapiano and Arkin*, 2009], India [*Nair et al*., 2009; *Rahman et al*., 2009, and China [*Yu et al*., 2009; *Zeng et al*., 2012; *Chen et al*., 2013a, 2013b].

China encompasses a range of climatic zones from maritime to continental climate and from monsoonal to semiarid and arid climate due to the unique topography and land-sea distribution [*Ding and Chan*, 2005; *Gao et al*., 2006]. Thus, the precipitation over China exhibits large spatial and temporal variability, indicating that comprehensive rainfall measurements are required to study the complicated changes in precipitation over China at different spatial and temporal scales. However, the number of rain gauges throughout China is small and unevenly distributed with sparse networks over western China [*Yu et al*., 2009], especially no gauges over west Tibetan Plateau and desert regions in Xinjiang province. Relative to the sparse ground gauge-based precipitation, the satellite precipitation products have incomparable superiority, particularly over the regions without rain gauges.

To increase the level of confidence in using the satellite precipitation estimates for different applications over China, some recent studies have been carried out to assess the applicability of different satellite precipitation products at basin [*Jiang et al*., 2010; *Yong et al*., 2010, 2012, 2013; *Chen et al*., 2011; *Liu et al*., 2012a; *Wu and Zhai*, 2012; *Zeng et al*., 2012; *Li et al*., 2013; *Yang and Luo*, 2014] and country-wide scales [*Xie et al*., 2007; *Yu et al*., 2009; *Zhou et al*., 2008; *Shen et al*., 2010; *Chen et al*., 2013b; *Qin et al*., 2014] using ground-based precipitation. However, the evaluations of satellite-derived products in these earlier studies are limited to relatively short period [*Xie et al*., 2007; *Yu et al*., 2009; *Shen et al*., 2010; *Chen et al*., 2013b; *Qin et al*., 2014; *Guo et al*., 2016] or some specific regions of China [*Jiang et al*., 2010; *Chen et al*., 2011; *Li et al*., 2013, 2014]. In addition, few studies have been carried out to evaluate the newly released satellite-derived precipitation products with much longer period over China; therefore, the long-term features of errors in the available latest satellite precipitation products over China are still unclear. The objective of this study is to evaluate the performance of five latest satellite precipitation products in detecting the quantity, spatiotemporal variation, amplitude and pattern of variability, rainy occurrence, and probability distribution function (PDF) of the precipitation amount for various intensities over China using ground gauge-based data from ~2400 stations with a time period of 2000–2014. Meanwhile, the systematic and random errors in the satellite precipitation estimates over China are also revealed. Findings in current study may provide the user community with some valuable and necessary information to choose suitable satellite-derived precipitation for their studies in China.

The data and methodology are introduced in section 2. The evaluation of each satellite precipitation product over China is presented in section 3. A summary of the results is provided in section 4.

2. Data and Methodology

2.1. Data

2.1.1. Satellite-Derived Precipitation Products

The satellite-derived precipitation products used in this study include CMORPH, PERSIANN, and TRMM TMPA precipitation data, which are introduced as follows.

CMORPH precipitation is derived by merging information from low orbiter satellite PM observations and geostationary satellite IR observations based on the morphing technique [*Joyce et al*., 2004]. These estimates are generated by algorithms of *Ferraro* [1997] for SSM/I, *Ferraro et al*. [2000] for AMSU-B, and *Kummerow et al*. [2001] for TMI. Compared to other merging methods, CMORPH adopts the IR data only to transport precipitation features identified and quantified from the PM data between periods when the PM data are not available at a particular position; the IR data are not used to produce any precipitation estimates [*Janowiak et al*., 2005; *Sapiano and Arkin*, 2009]. This technique can flexibly incorporate any precipitation estimates from any sources. Current study adopts the CMORPH precipitation data with the spatial resolution of 0.25° and temporal resolution of 3 h over a global latitude band of 60°N–60°S from 1 January 1998 to 31 December 2014 (ftp://ftp.cpc.ncep.noaa.gov/precip/CMORPH_V1.0/RAW/0.25deg-3HLY).

PERSIANN adopts an artificial neural network technique to estimate precipitation based on the geostationary satellite IR observations and low orbiter satellite PM observations [*Hsu et al*., 1997; *Sorooshian et al*., 2000; *Hong et al*., 2005]. The neural network calibrated with TMI, SSM/I, and AMSU data [*Janowiak et al*., 2001, 2005] is used to estimate 30 min precipitation rates from IR and visible imagery from geostationary satellites. The PERSIANN precipitation is generated from the IR-based precipitation estimates, which depend on the statistical relationships between IR estimates of cloud-top brightness temperature and mean precipitation rate and are calibrated and adjusted on the basis of PM data from low-orbital satellites using a neural network classification and/or approximation procedures [*Sorooshian et al*., 2000; *Shen et al*., 2010; *AghaKouchak et al*., 2011]. The surface type is included in the neural network and an adaptive process is adopted to iteratively adjust network parameters based on the error of the output compared to observations [*Hsu et al*., 1997; *Sorooshian et al*., 2000]. PERSIANN provides 3-hourly precipitation estimates on a 0.25° latitude/longitude grid over a global latitude band of 60°N–60°S from 1 March 2000 to 31 December 2014, which are available at ftp://persiann.eng.uci.edu/pub/PERSIANN/tar_3hr/.

The TRMM TMPA precipitation is derived by using an optimal combination of PM rain estimates from TMI, SSM/I, AMSR-E, and AMSU to adjust IR estimates from geostationary IR observations [*Kummerow et al*., 2000; *Huffman et al*., 2007; *Rozante et al*., 2010; *Liu et al*., 2012b] and computed for two products: (a) Near-real-time products are labeled as 3B40RT, 3B41RT, and 3B42RT, respectively. (b) Post real-time research quality product is labeled as 3B42 [*Kirstetter et al*., 2013; *Qin et al*., 2014]. The 3B40RT uses the high-quality PM data to produce precipitation estimates, while the 3B41RT adopts the PM-calibrated IR data to generate the precipitation estimates. The near-real-time product 3B42RT is generated by combining the PM observations (3B40RT) and the PM-calibrated geostationary IR data (3B41RT). The post real-time research product 3B42 is created similar to the near-real-time product 3B42RT, but the bias adjustments have been applied in the 3B42 precipitation product using the Global Precipitation Climatology Center (GPCC) monthly full/monitoring gauge analysis with 1° of horizontal resolution, in which about 500 gauge stations in China have been used [*Chen et al*., 2013b]. The newly released version 7 TRMM TMPA precipitation products used in current study include the near-real-time products TRMM3B41RTV7 and TRMM3B42RTV7 and the post

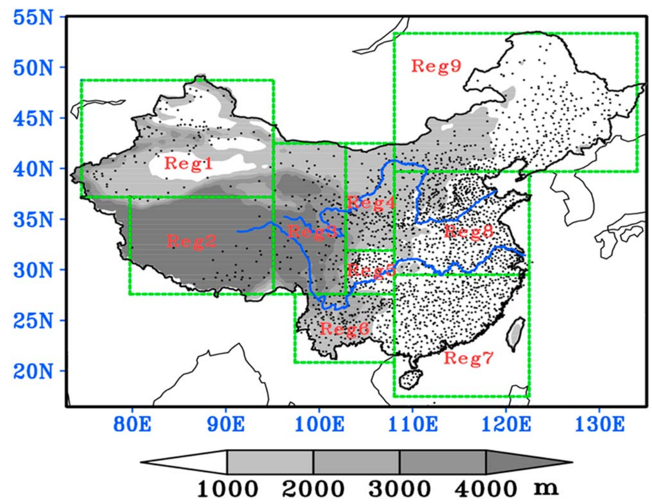

Figure 1. Locations (dark dots) of rain gauge stations in China in this study. Shadings show the terrain height over 1000 m. The Yangtze River and Yellow River are indicated by the blue curve lines. Nine subregions are denoted by the green rectangles.

real-time research quality product TRMM3B42V7. Compared to the data of version 6, the data of version 7 have been incorporated with the improved retrieval algorithms and more satellite data including enhanced TRMM Level-2 PR product, 0.07° Grisat-B1 infrared data, the Special Sensor Microwave Imager/Sounder (SSMIS) and Microwave Humidity Sounder (MHS), and the Meteorological Operational satellite program (MetOp) [*Chen et al*., 2013b; *Huffman and Bolvin*, 2013; *Kirstetter et al*., 2013; *Xue et al*., 2013; *Ochoa et al*., 2014; *Qiao et al*., 2014; *Liu*, 2015]. The TRMM3B41RTV7 data have the spatial resolution of 0.25° and temporal resolution of 1 h over a global latitude band of 60°N–60°S. The TRMM3B42RTV7 (TRMM3B42V7) provides 3-hourly precipitation estimates on a 0.25° latitude/longitude grid over a global latitude band of 60°N–60°S (50°N–50°S). The TRMM3B41RTV7 and TRMM3B42RTV7 cover the time period from 1 March 2000 to 31 December 2014, while TRMM3B42V7 covers the time period from 1 January 1998 to 31 December 2014; they are available at ftp://disc2.nascom.nasa.gov/data/TRMM/Gridded.

Among the five satellite precipitation products mentioned above, only TRMM3B42V7 adopts the bias adjustments using the GPCC gauge-based analysis of monthly precipitation, while the other four satellite precipitation products are based solely on satellite estimation.

2.1.2. Ground-Based Data Over China

The daily ground-based precipitation observed from 2479 stations in China (Figure 1) during 1951–2014, which is collected and quality controlled by the National Meteorological Information Center of the China Meteorological Administration, is used in current study. The gauge observed precipitation is used as the reference data to evaluate the performance of each satellite precipitation product. As shown in Figure 1, the rain gauge stations are densely (coarsely) distributed in the eastern (western) China, especially over west Tibetan Plateau, Tarim Basin, and Junggar Basin where rare stations are located.

2.2. Methodology

Because of the different time duration of the examined satellite products and the gauge data, we only assess the performance of each satellite precipitation product during 2000–2014. Considering the complications in comparing satellite estimated precipitation against gauge-based data due to the impact matching in space and time [*Serra and McPhaden*, 2003; *Bowman*, 2005], to easily validate the five satellite precipitation products, following *Chen et al*. [2013b], all satellite-derived precipitation products with the resolution of 1 h or 3 h were aggregated to daily temporal resolution. Meanwhile, the gauge data were interpolated onto the horizontal spatial resolution of 0.25° which is the same as the satellite data using the inverse distance weighting method [*Bartier and Keller*, 1996]. Note that we only gave the comparison between the satellite estimates and gauge observation when both satellite and gauge data were available at a given grid.

To reveal the consistencies of the five satellite precipitation products over China, we calculate the dispersion of the five satellite precipitation products according to the formula [*Huang et al*., 2014] given by

$$DS = \left\{ \sum_{l=1}^{m} \left(\frac{x_l - \bar{x}}{\bar{x}} \right)^2 \right\}^{1/2} \times 100\%, \tag{1}$$

where m (here $m = 5$) denotes the number of satellite precipitation products; x_l is the lth satellite product, and $\bar{x} = \frac{1}{m}\sum_{l=1}^{m} x_l$ is the mean of the m satellite precipitation products. D_S is an index measuring the spread and consistency of the multiple satellite products. High (low) D_S values indicate low (high) consistency among different products.

In this study, the temporal correlation is used to reveal the similarity of temporal variation between the satellite-derived precipitation and gauge-based data. The root-mean-square error (RMSE) is adopted to evaluate the performance of each satellite precipitation product in detecting the quantity. Meanwhile, the total error in the satellite precipitation estimates is separated into systematic and random error components based on the method suggested by *Willmott* [1981]. The formulas for these statistics are given as follows:

$$R = \frac{\sum_{i=1}^{N}\left(S_i - \overline{S}\right)\left(O_i - \overline{O}\right)}{\sqrt{\sum_{i=1}^{N}\left(S_i - \overline{S}\right)^2}\sqrt{\sum_{i=1}^{N}\left(O_i - \overline{O}\right)^2}} \tag{2}$$

$$\mathrm{RMSE} = \sqrt{\frac{1}{N}\sum_{i=1}^{N}\left(S_i - O_i\right)^2} \tag{3}$$

$$\frac{1}{N}\sum_{i=1}^{N}\left(S_i - O_i\right)^2 = \frac{1}{N}\sum_{i=1}^{N}\left(S_i^* - O_i\right)^2 + \frac{1}{N}\sum_{i=1}^{N}\left(S_i - S_i^*\right)^2, \tag{4}$$

where $S_i(O_i)$ is the satellite estimates (gauge observations) at N discrete points (in time and/or space) [*Taylor*, 2001], $\overline{S}$ ($\overline{O}$) is the mean value of satellite (gauge) data with a sample size of N. Temporal correlation (TC) is calculated based on equation (2). High TC indicates large similarity in temporal variation between the satellite precipitation estimates and gauge observations; while low RMSE indicates that the satellite estimates have close agreement with the gauge observations in quantity. The daily time series of S_i* in equation (4) is derived from the satellite estimates least squares linearly regressed against the gauge observation at each grid [*Willmott*, 1981; *Habib et al*., 2009; *Tian et al*., 2013]. $S_i* = b \times O_i + a$, a is the offset, b is a scale parameter representing the differences in the dynamic ranges between the gauge observations and the satellite estimates, both a and b deterministically specify the systematic error, and $\varepsilon_i = S_i - S_i^*$ is an instance of the random error which has zero mean [*Tian et al*., 2013]. The total mean square error (MSE) can be divided into systematic error (MSEs) and random error (MSEr) components represented by the first and second term at the right side of equation (4) [*Willmott*, 1981; *Habib et al*., 2009; *AghaKouchak et al*., 2012]. The MSEs is defined as the part of error to which a linear function can be fitted [*Willmott*, 1981]. Following *AghaKouchak et al*. [2012], the contribution of MSEs (MSEr) to MSE is given by MSEs/MSE × 100% (MSEr/MSE × 100%). In addition, the relative errors (RE = $(S - O)/O \times 100\%$, S and O are satellite estimates and gauge observations, respectively) are also used to evaluate the performance of satellite precipitation estimates in quantity.

To quantify the validation of satellite precipitation products in detecting both the amplitude and pattern of variability simultaneously, a measure of skill score suggested by *Taylor* [2001] is given by

$$T_s = \frac{4(1 + \mathrm{PC})}{(\sigma + 1/\sigma)^2(1 + \mathrm{PC}_0)} \tag{5}$$

$$\sigma = \sqrt{\frac{1}{N}\sum_{i=1}^{N}\left(S_i - \overline{S}\right)^2} \Bigg/ \sqrt{\frac{1}{N}\sum_{i=1}^{N}\left(O_i - \overline{O}\right)^2}, \tag{6}$$

where PC is the pattern correlation between the satellite estimates and gauge observation and is calculated based on equation (2) and PC_0 is an achievable maximum correlation (here set as 1). S_i (O_i) is the satellite (gauge) precipitation at the ith grid in a given domain. $\overline{S}$ and $\overline{O}$ are the satellite and gauge precipitation regionally averaged over the N grids in a given domain, respectively. σ is the spatial standard deviation of satellite precipitation normalized by that of gauge observation and reveals the similarity of the spatial heterogeneity between the simulation and observation [*Seo et al*., 2013; *Huang et al*., 2014]. T_s ranges from 0 to 1. The larger T_s is, the better performance of satellite-derived precipitation is [*Seo et al*., 2013; *Kan et al*., 2015].

Following the method suggested by *Su et al*. [2011], the probability of detection (POD) and false alarm ratio (FAR) based on a 2 × 2 contingency table (shown in Table 1) is used to evaluate the ability of satellite

Table 1. Contingency Table for Comparing Gauge-Based Precipitation and Satellite Precipitation

	Gauge ≥ Threshold	Gauge < Threshold
Satellite ≥ Threshold	a	b
Satellite < Threshold	c	d

precipitation products in detecting the occurrence of rainy events. As shown in Table 1, a is the number of hits, b is the number of false alarms, and c is the number of misses. The POD = $a/(a + c)$ and FAR = $b/(a + b)$ measure the fraction of the occurrence of rainy events that are correctly detected and false alarms [*Su et al.*, 2011; *Qin et al.*, 2014; *Yang and Luo*, 2014], respectively. It is obvious that perfect values for these scores are FAR = 0 and POD = 1.

To quantify the performance of satellite precipitation products over different regions of China, we divided the China mainland region into nine subregions with the consideration of the annual mean precipitation distribution, mountain ranges, elevations, and climate zones [*Ding and Chan*, 2005; *Gao et al.*, 2006]. The nine subregions shown in Figure 1 are Xinjiang (Reg1, 73°E–97°E, 37°N–48°N)

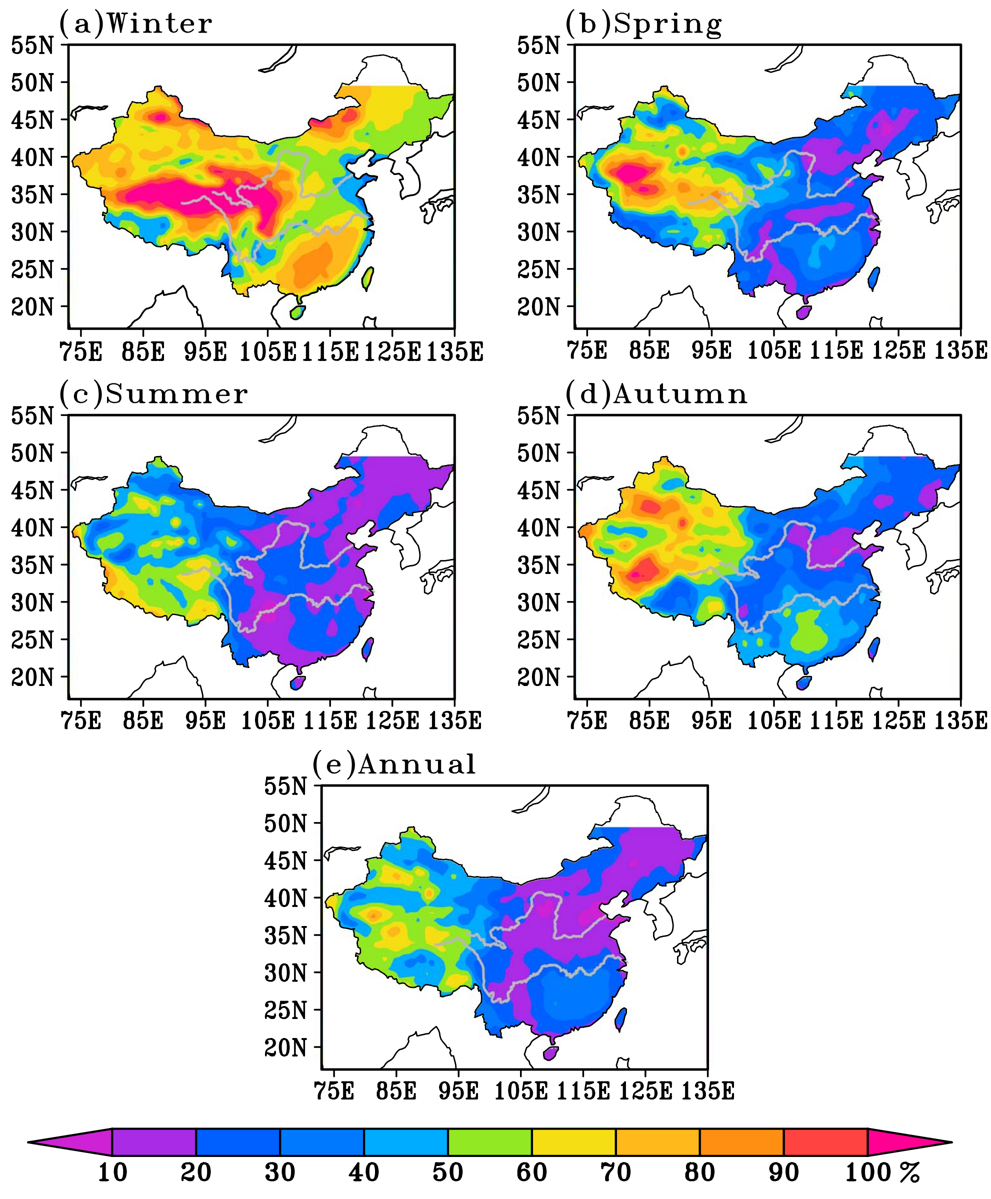

Figure 2. Spatial distribution of the D_S for the seasonal and annual mean precipitation averaged over 2000–2014 among the five satellite products.

characterized by semiarid to arid climate, central and western Tibetan Plateau (Reg2, 75°E–95°E, 28°N–37°N) with high altitude dominated by alpine climate, eastern Tibetan Plateau (Reg3, 95°E–103°E, 28°N–43°N) dominated by alpine semiarid to semihumid climate, upper reaches of the Yellow River valley (Reg4, 103°E–109°E, 33°N–43°N) with semiarid climate, Sichuan Basin (Reg5, 103°E–109°E, 28°N–33°N), Yungui Plateau (Reg6, 97°E–109°E, 22°N–28°N), southeastern China (Reg7, 109°E–122°E, 18°N–30°N), Jianghuai-northern China (Reg8, 109°E–122°E, 30°N–40°N), and northeastern China (Reg9, 109°E–135°E, 40°N–54°N). Regions 5–9 are characterized by monsoonal humid climate.

3. Results

To reveal the consistencies of the five satellite precipitation products over China, Figure 2 firstly gives the spatial distribution of the D_S for the seasonal and annual mean precipitation averaged over 2000–2014. For the climatic mean precipitation during the period of spring to autumn, the D_S values among the five satellite products are much lower over most eastern China than over northwestern China (Figures 2b–2d), indicating that the five products show relatively high (low) consistencies over eastern (northwestern) China from spring to autumn. Compared to the other seasons, the five satellite products exhibit much lower consistencies over most parts of China in winter (Figure 2a). Overall, the five satellite precipitation products display lower consistencies over the semiarid to arid regions in western China than over humid regions in eastern China in all seasons. In addition, the five satellite products display the highest (lowest) consistencies in summer (winter) among the four seasons over most China. In the following sections, detailed comparison of each satellite precipitation product's performance over China and each subregion are further conducted.

3.1. Climatic Mean Precipitation Over 15 Years

Figure 3 gives the spatial distribution of the seasonal and annual climatic mean precipitation over China during 2000–2014. The ground gauge-based precipitation over China displays distinct seasonal variations (Figures 3f1–3f4): The precipitation increases from winter to summer and then decreases in autumn. A strong rainfall center with the intensity over 1.5 mm d^{-1} in winter and 4.5 mm d^{-1} in spring is located in southeastern China. Strong rainfall centers with the intensity above 7.5 mm d^{-1} in summer are located in southern Yunan province and coastal regions of southern China. Large rainfall centers over 3.5 mm d^{-1} in autumn can be seen in the coastal regions of southern China and middle Yangtze River valley. Compared to the gauge observation, all of the five satellite precipitation products can basically capture the seasonal variations of precipitation over China (Figures 3a1–3e4). In general, TRMM3B42V7 tends to show much better agreement with the gauge-based data in different seasons relative to the other four satellite products.

The gauge-based data show that the annual mean precipitation over China gradually decreases from southeastern China to northwestern China (Figure 3f5). The annual mean precipitation over 2.5 mm d^{-1} (below 1.5 mm d^{-1}) is located in southeastern (northwestern and northeastern) China. Meanwhile, two strong rainfall centers above 4.5 mm d^{-1} can be seen over the coastal regions of southern China and south of the lower reaches of the Yangtze River valley. All of the five satellite products can basically capture the overall spatial distribution of the gauge-based annual mean precipitation over China (Figures 3a5–3e5). However, CMORPH, PERSIANN, and TRMM3B41RTV7 (Figures 3a5–3c5) show underestimation over southeastern China. Precipitation over the Tibetan Plateau and Tianshan is overestimated by PERSIANN, TRMM3B41RTV7, and TRMM3B42RTV7 (Figures 3b5–3d5). Despite the fact that the annual mean precipitation over southeastern China is overestimated by TRMM3B42RTV7, the locations of the two strong rainfall centers over the coastal regions of southern China and south of the lower reaches of the Yangtze River valley are accurately detected (Figure 3d5). Compared to the other four satellite products, TRMM3B42V7 exhibits much closer agreements with the gauge observed annual mean precipitation in terms of spatial pattern and quantity (Figure 3e5).

The relative biases of the satellite precipitation estimates can be further clearly indicated by Figure 4. As shown in Figures 4a–4e, CMORPH tends to underestimate (overestimate) the seasonal and annual climatic mean precipitation over southeastern and northeastern China (most western China). The summer, autumn, and annual precipitation over Tarim Basin and surrounding areas from CMORPH is overestimated by more than 80%. From Figures 4f–4j, the relative errors of PERSIANN precipitation vary seasonally. The winter precipitation from PERSIANN is underestimated by more than 60% over southern China and overestimated by more than 80% over

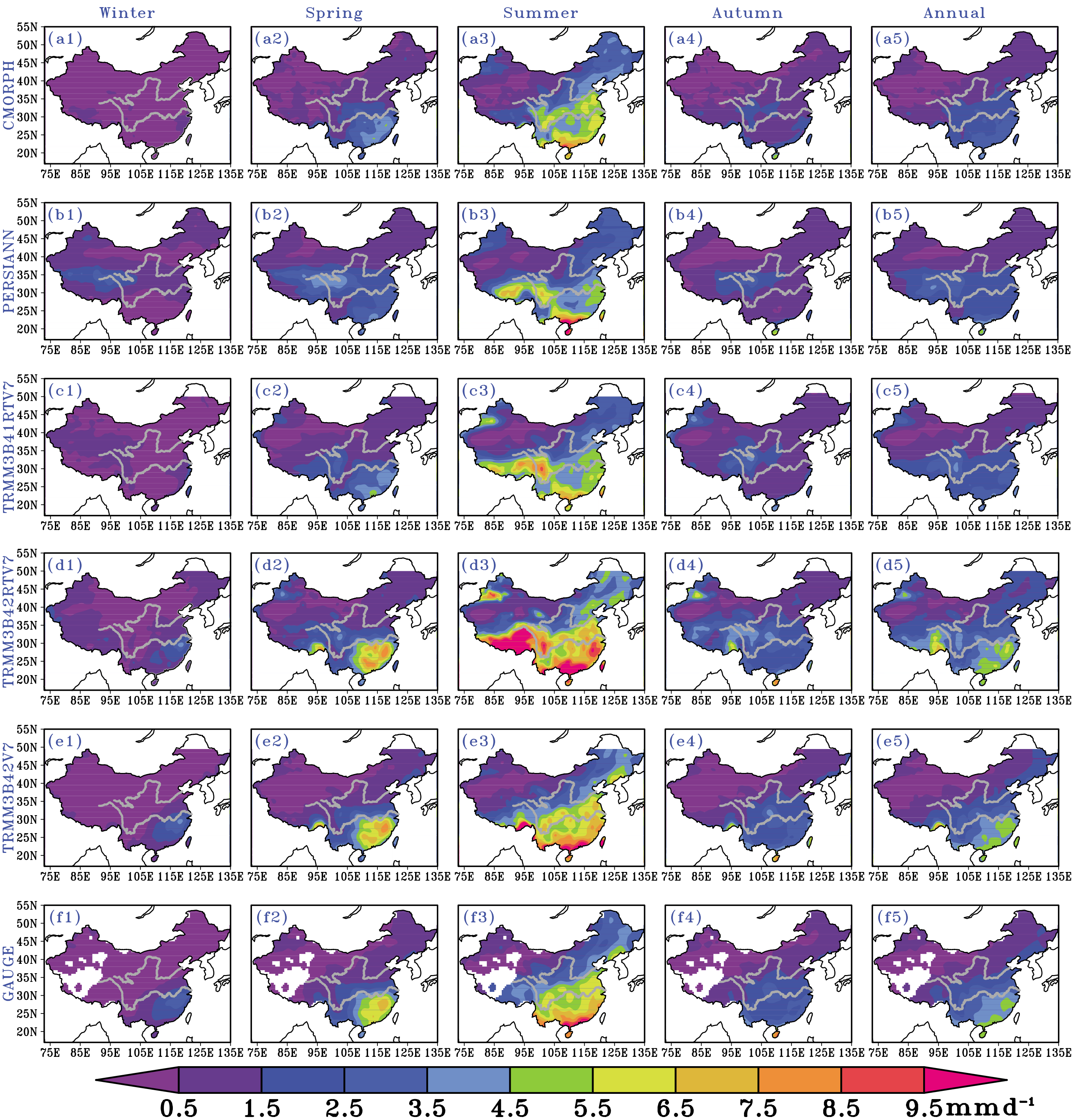

Figure 3. Spatial distribution of the seasonal and annual climatic mean precipitation from each satellite product and gauge observation during 2000–2014.

the other parts of China. From winter to summer, the scopes of the overestimation (underestimation) by PERSIANN shrink (expand) from northeastern China to northwestern China (from southeastern China to northeastern China). The relative errors over most China for PERSIANN are the smallest in summer among the four seasons. The relative errors in TRMM3B41RTV7 show very similar features to those of PERSIANN (Figures 4k–4o). As shown in Figures 4p–4t, the TRMM3B42RTV7 tends to overestimate the seasonal and annual precipitation over

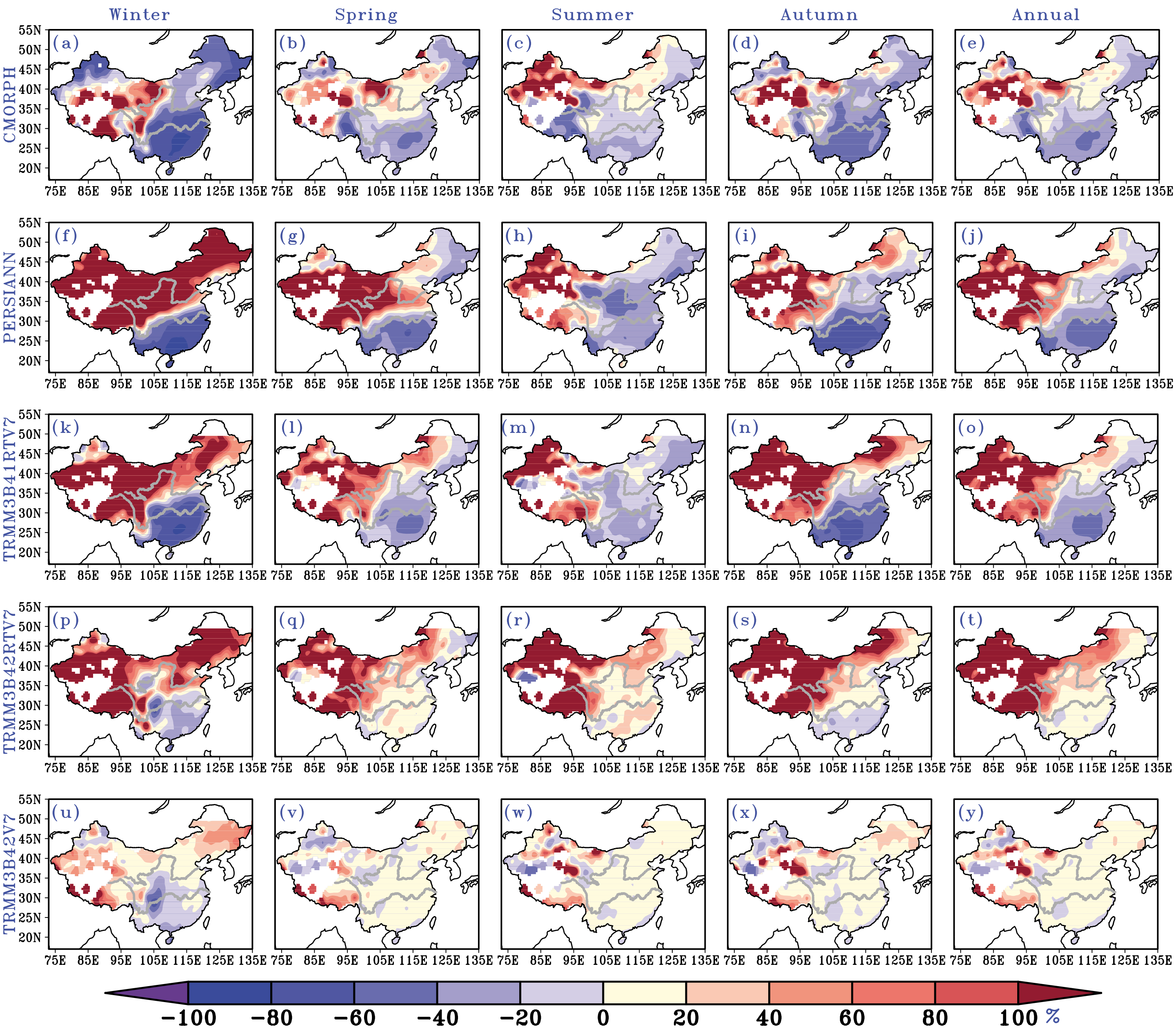

Figure 4. Spatial distribution of the relative errors of the seasonal and annual climatic mean precipitation from each satellite product during 2000–2014.

most parts of China with much larger errors over northwestern to northeastern China and the Tibetan Plateau, except that the precipitation over some parts of southeastern China is underestimated during winter and autumn. The relative errors in the annual precipitation of TRMM3B42V7 over most parts of eastern China range from 0 to 20% (Figure 4y). However, much larger relative errors in the TRMM3B42V7 annual precipitation can be found over northwestern China: TRMM3B42V7 overestimated the precipitation by more than 40% over the Tarim Basin, south, and northeast edges of the Tibetan Plateau, while the precipitation over the Tianshan and northwest edge of the Tibetan Plateau is underestimated by more than 40%. The large biases in TRMM3B42V7 precipitation over western China may be attributed to the sparse ground gauge-based information adopted in the GPCC data for the bias adjustments. The relative errors of TRMM3B42V7 from spring to autumn (Figures 4v–4x) display very similar features to those of the annual precipitation (Figure 4y). From Figure 4u, TRMM3B42V7 overestimates the winter precipitation over large parts of China except southern China and Tianshan where the precipitation is underestimated. Large relative errors of the winter precipitation can be noted over Xinjiang province, the

Tibetan Plateau, northeastern China, and Shichuan Basin. Over the other parts of China the relative errors of TRMM3B42V7 precipitation in winter range from −20% to 20%.

From Figure 4, TRMM3B42RTV7 and TRMM3B42V7 show much smaller underestimation of precipitation over south and southeastern China in winter compared to CMORPH, PERSIANN, and TRMM3B41RTV7. The large underestimation in CMORPH, PERSIANN, and TRMM3B41RTV7 precipitation over southern and southeastern China from spring to summer is not visible in TRMM3B42RTV7 and TRMM3B42V7 products which show slight overestimation, indicating significant improvements in the TRMM3B42RTV7 and TRMM3B42V7 products over these regions. The large overestimation of all satellite products in cool and cold seasons (late autumn to early spring) over the high latitudes of China dominated by arid to semiarid climate (i.e., northwestern China and west part of northeastern China) and the Tibetan Plateau featured by alpine climate is mainly associated with the imperfect screening of the cold surface from the IR images and the impact of surface snow cover and ice particles on the PM retrievals [*Shen et al.*, 2010; *Yong et al.*, 2012, 2013]. The IR-based estimates have very poor ability in detecting the warm-top stratiform cloud systems in the cold seasons [*Dinku et al.*, 2007; *Tian et al.*, 2007], and the PM retrievals might detect more scattering related to the frozen land surface and ice particles in atmosphere during cold seasons [*Vila et al.*, 2007; *Bookhagen and Burbank*, 2010; *Kidd et al.*, 2012; *Chen et al.*, 2013b; *Qin et al.*, 2014], leading to overestimated precipitation [*Hirpa et al.*, 2010; *Yong et al.*, 2010; *Gebregiorgis and Hossain*, 2013; *Nasrollahi et al.*, 2013], and further impact on the calibration precision of the IR data [*Yong et al.*, 2013]. Thus, the available PM-calibrated IR and the PM data themselves tend show large overestimation over the high-latitude regions and the Tibetan Plateau with high altitude in cold seasons [*Chen et al.*, 2013b; *Yong et al.*, 2013]. In addition, the overestimation in the satellite precipitation over the arid and semiarid inland regions of northwestern China may also be attributed to that the evaporation of raindrops in the dry atmosphere before reaching the surface is not well considered in the retrieval algorithms [*McCollum et al.*, 2000; *Qin et al.*, 2014].

Overall, the relative errors of the five satellite precipitation products vary regionally and seasonally. All the five satellite products display larger relative errors over northwestern and northeastern China than over southeastern China. The relative errors of all satellite rainfall estimates over most parts of China appear to be much larger in winter than in the other seasons; this is one of the limitations and common features of current satellite-based precipitation data sets [*Sorooshian et al.*, 2011; *Yang and Luo*, 2014; *Qin et al.*, 2014]. Among the five satellite products, TRMM3B42V7 shows the smallest relative errors over most parts of China in all seasons (Appendix A).

To quantify the performance of each satellite product in different subregions of China, the skill score T_s indicated by equation (5) is used to evaluate the ability of the satellite precipitation products in detecting both the amplitude and pattern of variability [*Taylor*, 2001]. TRMM3B42V7 basically shows the highest T_s score among the five satellite products (Figure A1), suggesting that it has the best ability in detecting the amplitude and pattern of variability for the seasonal and annual climatic mean precipitation over each subregion of China. Meanwhile, TRM3B42RTV7 shows the second best performance over almost all subregions of eastern China (Regions 5–9) among the five satellite products.

3.2. Daily Precipitation

The spatial distribution of the TC and RMSE for each satellite product by comparing the daily satellite precipitation with the gauge-based data during 2000–2014 is shown in Figure A2, each satellite precipitation product produces reasonable TC over most parts of China especially southeastern China where the TC values are above 0.5. However, TC values over the extreme arid areas like the Tarim Basin are even less than 0.1. Meanwhile, TRMM3B42RTV7 and TRMM3B42V7 show very comparable spatial patterns and quantity of TC. TC values for both TRMM3B42RTV7 and TRMM3B42V7 above 0.7 are located lover the coastal regions in southeastern China. Among the five satellite products, TRMM3B42V7 tends to show the best performance in depicting the temporal variation of precipitation over most parts of China; meanwhile, TRMM3B42RTV7 appears to show the second best ability in reproducing the temporal variation of precipitation over most parts of eastern China (Regions 5–9). This can be further indicated by Figures 5a–5d.

All of the satellite precipitation products show very similar distribution of RMSE with larger values over southeastern China than over northwestern China (Figures A2f–A2j of the appendix). The reasons behind this can be attributed to the fact that the systematic biases of satellite precipitation are proportional to the rain rate magnitude [*Habib et al.*, 2009; *AghaKouchak et al.*, 2012]. From Figures 5e–5h, the CMORPH and TRMM3B42V7 show very comparable RMSE over each subregion in different seasons, although TRMM3B42V7 exhibits

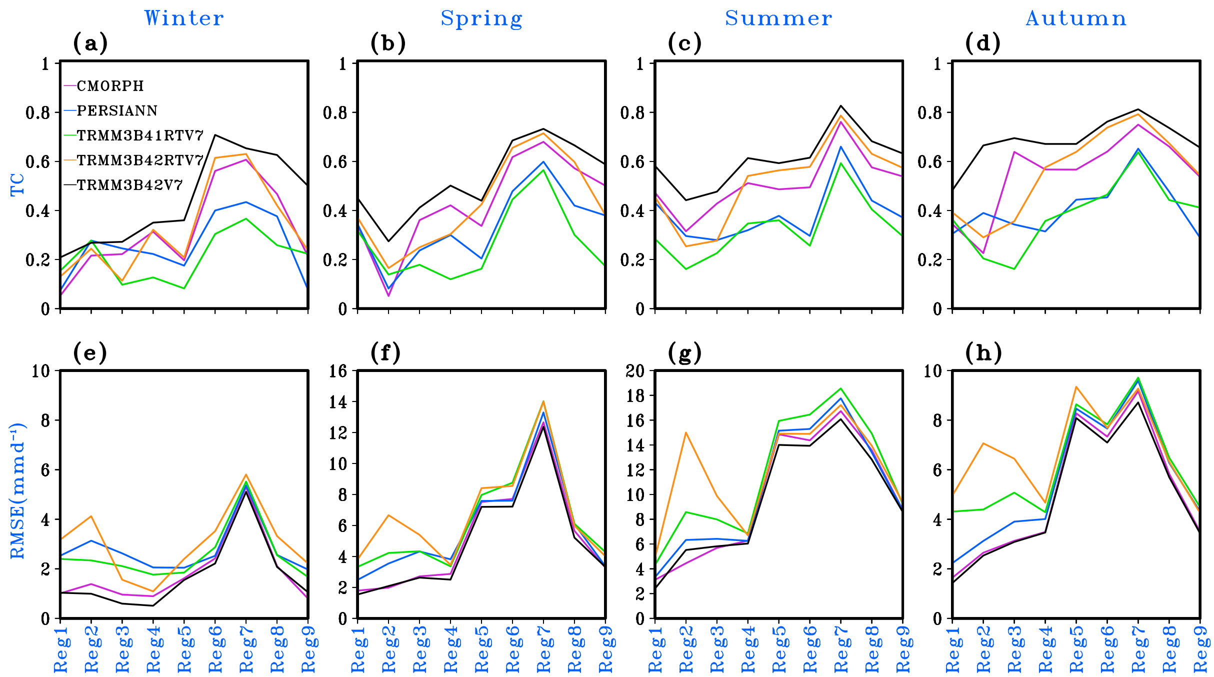

Figure 5. Domain averaged TC and RMSE for each satellite precipitation product during 2000–2014 over each subregion of China in different seasons.

relatively lower RMSE. Among the five satellite products, TMM3B42RTV7 shows the highest RMSE over northwestern China (Regions 1–4). The RMSE differences among the five satellite products are much smaller over humid regions (i.e., Regions 5–9) than over semiarid to arid regions (i.e., Regions 1–4) in all seasons. Among the five satellite products, TRMM3B42V7 exhibits the smallest RMSE over most subregions of China in different seasons, indicating the best agreement with the gauge observation in quantity.

In addition to the evaluation of each satellite product's performance in depicting the agreement in the temporal variation and quantity, Figure 6 further exhibits the daily multiyear mean T_s derived from the daily T_s during 2000–2014 to show the agreement in the amplitude and pattern of variability [*Taylor*, 2001]. The performance of each satellite precipitation product in detecting the amplitude and pattern of variability over each subregion vary seasonally with larger T_s values in mild and warm seasons (May to October) than in cool and cold seasons (November to April). Over the semiarid to arid regions and high-altitude regions (i.e., Regions 1–3), CMORPH and TRMM3B42V7 show comparable T_s in most time of a year (Figures 6a–6c). However, TRMM3B42RTV7 and TRMM3B42V7 show very close T_s over the humid regions (i.e., Regions 5–9) (Figures 6e–6i). TRMM3B41RTV7 and PERSIANN show comparable T_s over Regions 5–9 during most time of a year; they display much weaker ability over these regions compared to the other three products. Among the five satellite products, TRMM3B42V7 shows the highest performance in reproducing the amplitude and pattern of variability of precipitation over each subregion of China in most time of a year.

Overall, according to the various verification statistics including TC, RMSE, and T_s, TRMM3B42V7 shows the highest agreement with the gauge-based precipitation in quantity, temporal variation, and amplitude and pattern of variability over most subregions of China among the five satellite products. This may be attributed to the application of bias adjusted by the gauge observations [*Chen et al.*, 2013b; *Huffman and Bolvin*, 2013], which can significantly remove the large-scale errors [*Shen et al.*, 2010; *Qin et al.*, 2014]. Meanwhile, the near-real-time product TRMM3B42RTV7 with the applications of improved retrieval algorithms and more satellite data [*Chen et al.*, 2013b; *Huffman and Bolvin*, 2013; *Kirstetter et al.*, 2013; *Xue et al.*, 2013] shows the second best ability over eastern China among the five satellite products.

3.3. Error Characteristics of Daily Satellite-Based Precipitation

To reveal the detailed features of the errors in the satellite precipitation estimates, the systematic and random errors (see equation (4) in section 2.2) [*Willmott*, 1981] of each satellite precipitation product across China

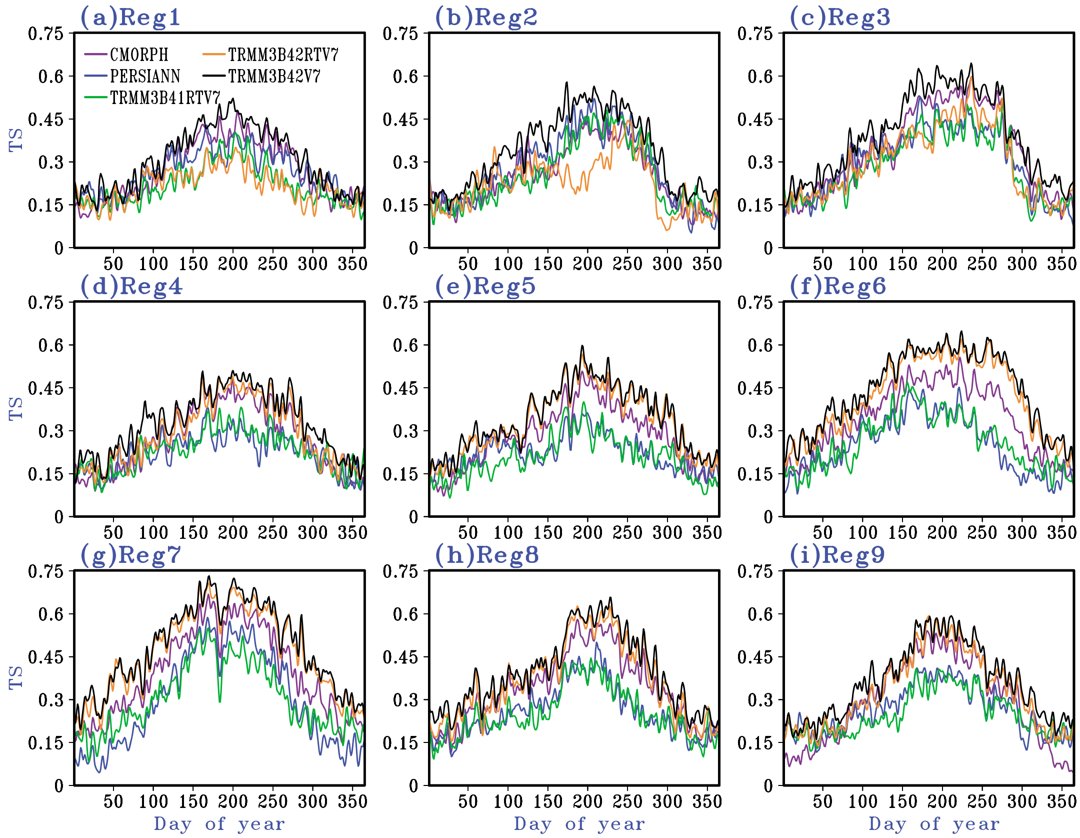

Figure 6. Daily time series of the T_S for each satellite precipitation product over each subregion of China averaged over 2000–2014.

are further analyzed in this section. Figure 7 gives the systematic error and the differences between the systematic error and the random error for the daily satellite precipitation data during 2000–2014. As shown in Figure 7a, CMORPH shows relatively larger systematic error (relative to the total error) over south Tibetan Plateau and most southeastern China than over most Xinjiang province, northern, and northeastern China. Both PERSIANN and TRMM3B41RTV7 exhibit less systematic error over western China than over eastern China; the strong systematic error above 50% can be seen in central to southeastern China (Figures 7b and 7c). As shown in Figure 7d and 7e, the values of systematic error for TRMM3B42RTV7 and TRMM3B42V7 across China are less than 40%. Compared to CMORPH, PERSIANN, and TRMM3B41RTV7, both TRMM3B42RTV7 and TRMM3B42V7 significantly reduce the systematic error over most China especially over southeastern China, this behavior may be associated with the adoption of the improved retrieval algorithms and more satellite data [*Huffman and Bolvin*, 2013; *Kirstetter et al.*, 2013; *Xue et al.*, 2013; *Ochoa et al.*, 2014; *Qiao et al.*, 2014; *Liu*, 2015].

From Figure 7f, the systematic error for CMORPH is less (larger) than the random error component over most northwestern and northeastern China and Sichuan Basin (south Tibet, Yunnan province, and southeastern China). The systematic error for both PERSIANN and TRMM3B41RTV7 is smaller (larger) than the random error over most eastern (western) China (Figures 7g and 7h). However, both TRMM3B42RTV7 and TRMM3B42V7 exhibit significantly less systematic error than the random error component across China (Figures 7i and 7j), indicating that the uncertainties in the TRMM3B42RTV7 and TRMM3B42V7 precipitation estimates are remarkably reduced compared to the other three satellite products.

In addition to the spatiotemporal variability of error, bias adjustment algorithms should take into account the distribution of total error [*AghaKouchak et al.*, 2012]. It is clear that all satellite precipitation estimates show that the PDF of the total error decreases with the error increased (Figure A3a). TRMM3B42V7 (TRMM3B41RTV7) displays the best (worst) performance among the five satellite products (Figure A3b). Meanwhile, CMORPH and TRMM3B42RTV7 show very comparable cumulative distribution function (CDF) of total error, although TRMM3B42RTV7 is slightly better. To much better compare the performance, a set

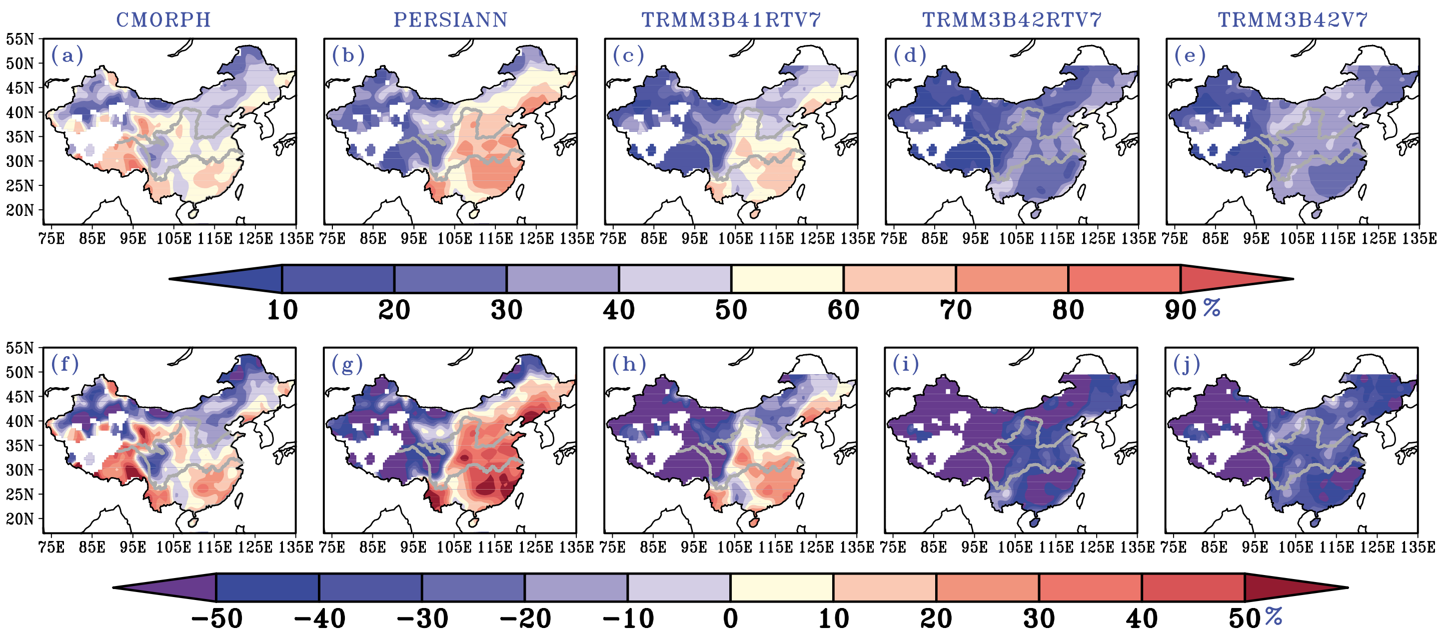

Figure 7. (a–e) Spatial distribution of the systematic error and (f–j) the differences between the systematic error and the random error for the daily precipitation data from each satellite product during 2000–2014.

of quantitative numbers for the assessment are given as follows: the absolute bias below 1 mm d^{-1} for CMORPH, PERSIANN, TRMM3B41RTV7, TRMM3B42RTV7, and TRMM3B42V7 accounts for 41.59%, 37.36%, 37.59%, 43.68%, and 48.37% of the total error, respectively.

3.4. Performance of Each Satellite Product in Detecting the Rainy Events

Figure 8 gives the spatial distribution of POD and FAR with the threshold of 1 mm d^{-1}. All satellite-derived data exhibit much higher POD (lower FAR) values over southeastern China than over northwestern China, indicating that each satellite product has better performance in detecting the occurrence of rainy events over southeastern China than over northwestern China. Compared to the other three satellite products, TRMM3B42RTV7 and TRMM3B42V7 show higher POD (lower FAR) values over most parts of China, suggesting better performance in detecting the occurrence of rainy events with the rain rate above 1 mm d^{-1}.

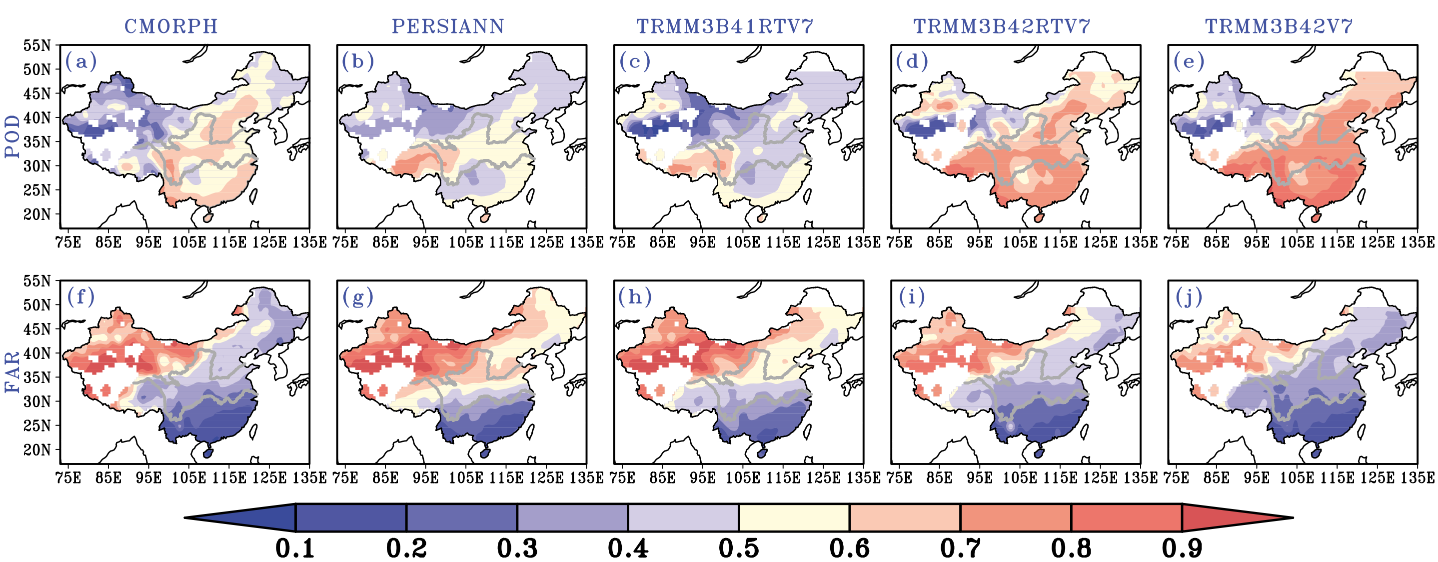

Figure 8. Spatial distribution of POD and FAR with the threshold of 1 mm d^{-1} for each satellite precipitation product during 2000–2014.

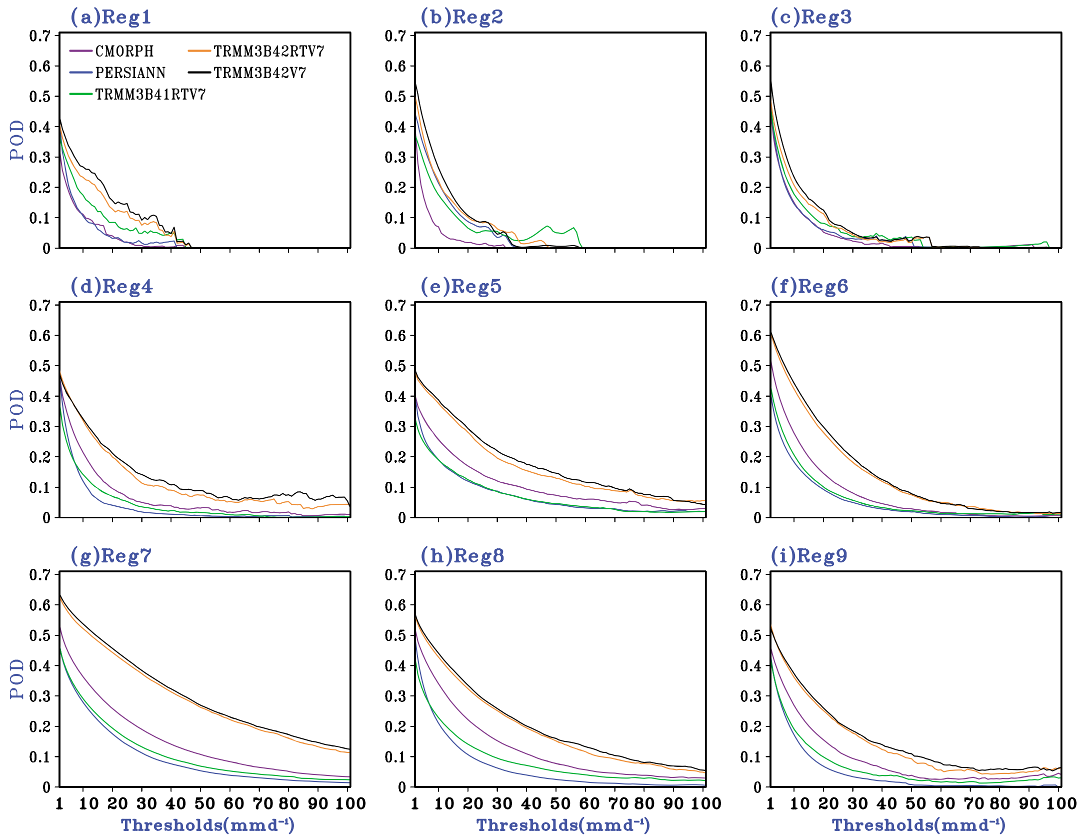

Figure 9. The POD for different precipitation thresholds ranging from 1 to 100 mm d^{-1} with a 1 mm d^{-1} interval for each satellite precipitation product over the nine subregions of China during 2000–2014.

To evaluate the performance of the satellite estimates for light to heavy rainfall events over each subregion, Figure 9 further displays the POD for the different daily precipitation thresholds ranging from 1 to 100 mm d^{-1} with a 1 mm d^{-1} interval over the nine subregions of China during 2000–2014. All satellite products tend to show decreased POD with the precipitation threshold increased over all subregions of China, indicating that the performance of each satellite product in detecting the rain occurrence weakens with the precipitation threshold enhanced, this is consistent with the findings of earlier studies [*AghaKouchak et al.*, 2011; *Mehran and AghaKouchak*, 2014]. TRMM3B42RTV7 and TRMM3B42V7 exhibit comparable POD; rain occurrence for each precipitation threshold is obviously better detected by TRMM3B42RTV7 and TRMM3B42V7 over each subregion of China especially over eastern China (Figures 9d–9i) relative to the other three products. CMORPH appears to exhibit moderate skill in detecting the rain occurrence with different precipitation thresholds over eastern China among the five satellite products. Overall, TRMM3B42V7 (PERSIANN) tends to show the best (worst) skill in detecting the occurrence of rainy events with different precipitation thresholds over most parts of China among the five satellite precipitation products.

Figure 10 exhibits the PDF by precipitation amount for different rain rates over each subregion of China during 2000–2014. TRMM3B42V7 and CMORPH show much better agreement with the gauge-based data relative to the other three satellite products over Xinjiang (Figure 10a), although they slightly overestimate (underestimate) the precipitation for the rates less (more) than 8 mm d^{-1}. However, PERSIANN, TRMM3B41RTV7, and TRMM3B42RTV7 appear to yield much more precipitation amount for the rates above 2 mm d^{-1} over Xinjiang, leading to the large overestimated annual precipitation (Figures 4j, 4o, and 4t). As shown in Figures 10b and 10c, TRMM3B42V7 appears to show the closest agreement with the gauge observed precipitation amount for different rain rates over the Tibetan Plateau among the five satellite products. Meanwhile, TRMM3B41RTV7 and TRMM3B42RTV7 tend to largely overestimate the precipitation amount for the rates above 16 mm d^{-1} over the Tibetan Plateau (Figures 10b and 10c), leading to large overestimation in the annual precipitation (Figures 4o and 4t). Figures 10a–10c show that most satellite

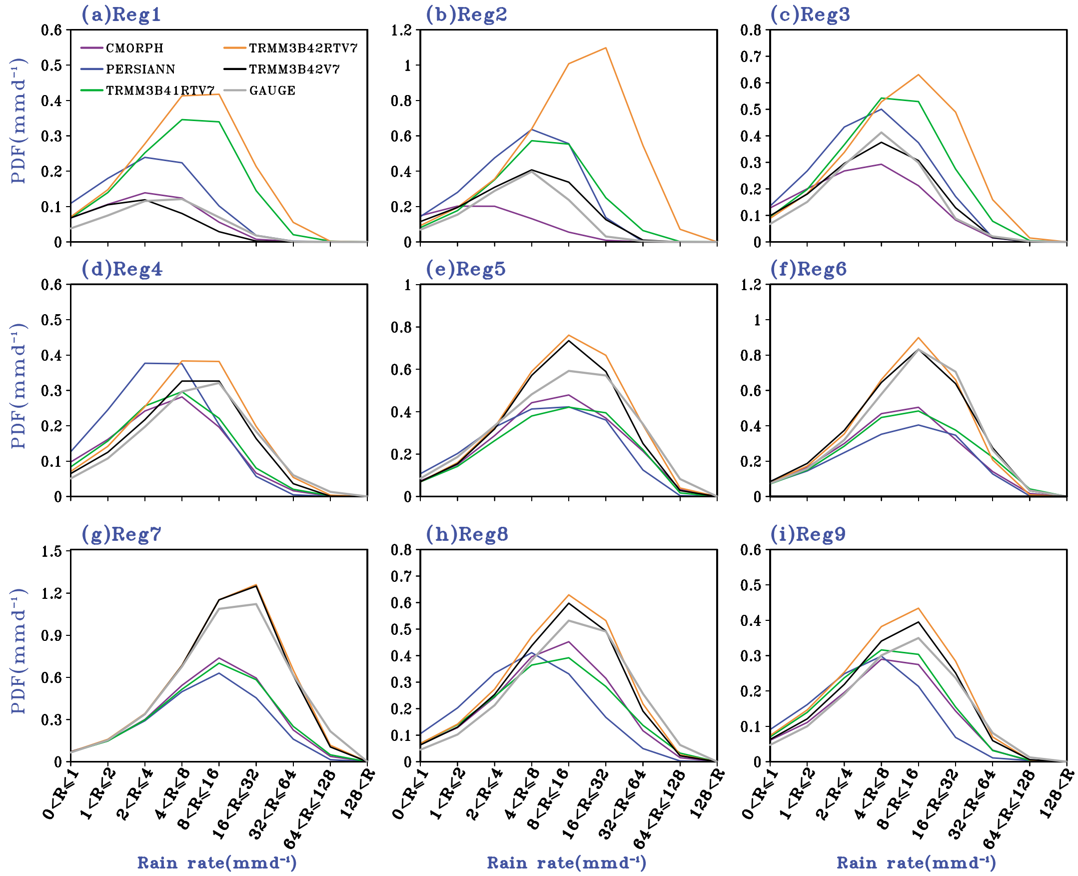

Figure 10. PDF of the precipitation amount with different rain rates for each satellite precipitation product over 2000–2014.

precipitation products still face a great challenge to accurately estimate the precipitation over high-altitude mountainous region and remote desert areas, which can be also seen in Figure 4. Over the regions characterized by monsoonal humid climate (Figures 10e–10i), all satellite products tend to show better performance in detecting the light precipitation with the rain rates below 8 mm d^{-1} relative to the moderate to heavy precipitation with the rain rates above 8 mm d^{-1}. Both TRMM3B42V7 and TRMM3B42RTV7 show comparable ability over these regions, despite that TRMM3B42V7 shows relatively better performance. In addition, the large underestimation for the precipitation rates between 16 and 128 mm d^{-1} in CMORPH, PERSIANN, and TRMM3B41RTV7 over Regions 5–9, which may lead to the underestimated annual precipitation over southern and eastern China (Figures 4e, 4j, and 4o). Overall, according to the statistics of PDF by the precipitation amount of different rain rates, TRMM3B42V7 (TRMM3B42RTV7) shows the best (second best) agreement with the gauge observation over most parts of China (eastern China) among the five satellite products.

The analysis mentioned above suggests that the satellite precipitation estimates generally show very poor performance in cold seasons. To illustrate the possible reasons, we further evaluate the performance of the satellite products in detecting the snow and rainfall in winter. The RMSE and POD with the threshold of 1 mm d^{-1} of snow and rainfall in winter for each satellite precipitation product regionally averaged over each subregion of China during 2000–2014 are given in Figure 11. All satellite products consistently show much larger RMSE of snow than that of rainfall over northwestern (Regions 1–4) and northeastern (Region 9) China where the snow often happens during cold seasons, and each satellite product exhibits lower POD in detecting snow events than rainfall events over almost all subregions of China, suggesting that all satellite products tend to display worse performance in detecting snow relative to rainfall. Possible reasons may be attributed to the interference of ice in atmosphere, surface snow cover, and land surface properties to PM and IR retrievals [*Grody and Weng*, 2008; *Yong et al.*, 2012; *Chen et al.*, 2013b], PM retrievals might detect more scattering associated with the frozen land surface and ice particles in atmosphere [*Bookhagen and Burbank*,

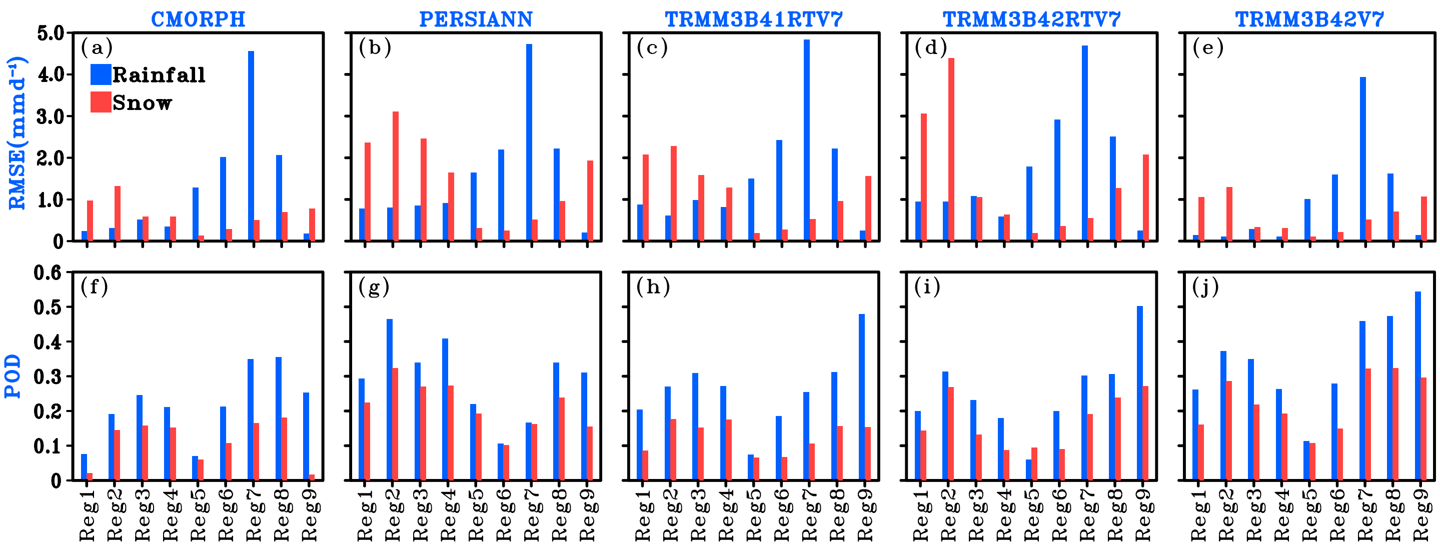

Figure 11. The RMSE and POD with the threshold of 1 mm d^{-1} of snow and rainfall in winter for each satellite precipitation product regionally averaged over each subregion of China during 2000–2014.

2010; *Kidd et al*., 2012; *Chen et al*., 2013b], and the emissivity signal from lower surface temperature at high-altitude regions may be identified as rain by IR retrievals [*Kidd et al*., 2012; *Gebregiorgis and Hossain*, 2013; *Nasrollahi et al*., 2013; *Qin et al*., 2014]; these may lead to the precipitation overestimation over most northwestern China and the Tibetan Plateau.

4. Concluding Remarks and Discussions

The performance of the five satellite products including CMORPH, PERSIANN, TRMM3B41RTV7, TRMM3B42RTV7, and TRMM3B42V7 over China has been systematically examined during the period of 2000–2014 using the daily gauge-based data in terms of the climatic mean, daily time series, systematic and random errors, PDF and CDF of total error, POD and FAR of the occurrence of rainy events for different precipitation thresholds, and PDF of the precipitation amount for different rain rates. The main results can be summarized as follows:

All of the five satellite precipitation products can basically capture the overall spatial distribution of the annual and seasonal climatic mean precipitation over China. Satellite precipitation estimates generally show better performance in warm seasons than in cold seasons. They also exhibit higher ability over humid regions than over semiarid to arid regions. All satellite products show better skill in detecting the light precipitation with the rates less than 8 mm d^{-1} than the moderate to heavy precipitation over eastern China. The large underestimation of the precipitation amount for the rain rates between 16 and 128 mm d^{-1} in CMORPH, PERSIANN, and TRMM3B41RTV7 over most parts of eastern China does not appear in TRMM3B42RTV7 and TRMM3B42V7. Both TRMM3B42RTV7 and TRMM3B42V7 exhibit obviously less systematic error than the random error component across China, indicating reduced uncertainties in the TRMM3B42RTV7 and TRMM3B42V7 products relative to the other three satellite products. Among the five satellite products, TRMM3B42V7 shows the best agreement with the gauge-based data in terms of the spatiotemporal variation, amplitude and pattern of variability, occurrence of rainy events for different thresholds, and PDF of the precipitation amount for different rain rates over most parts of China; TRMM3B42RTV7 appears to display the second best performance over most subregions of eastern China.

The analysis from all verification statistics in current study suggests that the satellite-derived precipitation generally perform better in warm seasons than in cold seasons, and better performance is found over humid regions than over arid and alpine regions. This may be attributed to that the satellite-retrieved precipitation is closely related to the precipitation types and intensities [*Beighley et al*., 2011; *Kidd et al*., 2012; *Qin et al*., 2014; *Sorooshian et al*., 2011]. Further analysis of snow versus rainfall in terms of accuracy of the satellite estimates suggests that all satellite products tend to show worse performance in detecting snow relative to rainfall over China especially over northwestern and northeastern China with high latitudes. Meanwhile, the satellite

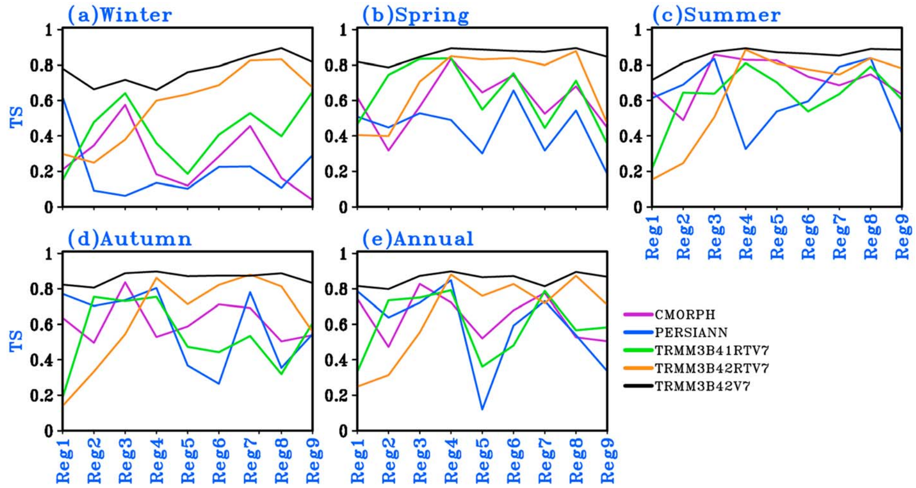

Figure A1. T_S for each satellite product in detecting the amplitude and pattern of variability of the seasonal and annual climatic mean precipitation over each subregion of China.

rainfall estimates tend to show worse performance over high-altitude regions (i.e., Tibetan Plateau) relative to low-altitude regions of China. This may be resulted from the elevation effect and impact of the ice/snow covered surfaces [*Giovannettone and Barros*, 2009; *Gebregiorgis and Hossain*, 2013; *Nasrollahi et al.*, 2013; *Qin et al.*, 2014; *Yang and Luo*, 2014; *Guo et al.*, 2016]. *Shen et al.* [2010] has shown that CMORPH precipitation product exhibits the best performance in depicting the spatial pattern and temporal variations of precipitation over China among six satellite products (CMORPH, PERSIANN, TRMM3B42RTV6, TRMM3B42V6, NRL, and MWCOMB). However, current study indicates that the research product TRMM3B42V7 performs the best at almost all aspects of precipitation among the five satellite products. The differences between the current and previous studies may be resulted from the improvements of TRMM3B42V7 upon TRMM3B42V6 [*Chen et al.*, 2013b]. It is noted that TRMM3B42V7 precipitation still shows large bias over western China especially over the desert regions and west Tibetan Plateau due to sparse ground gauges which are used in the GPCC data for the bias adjustments. To further improve the quality of the

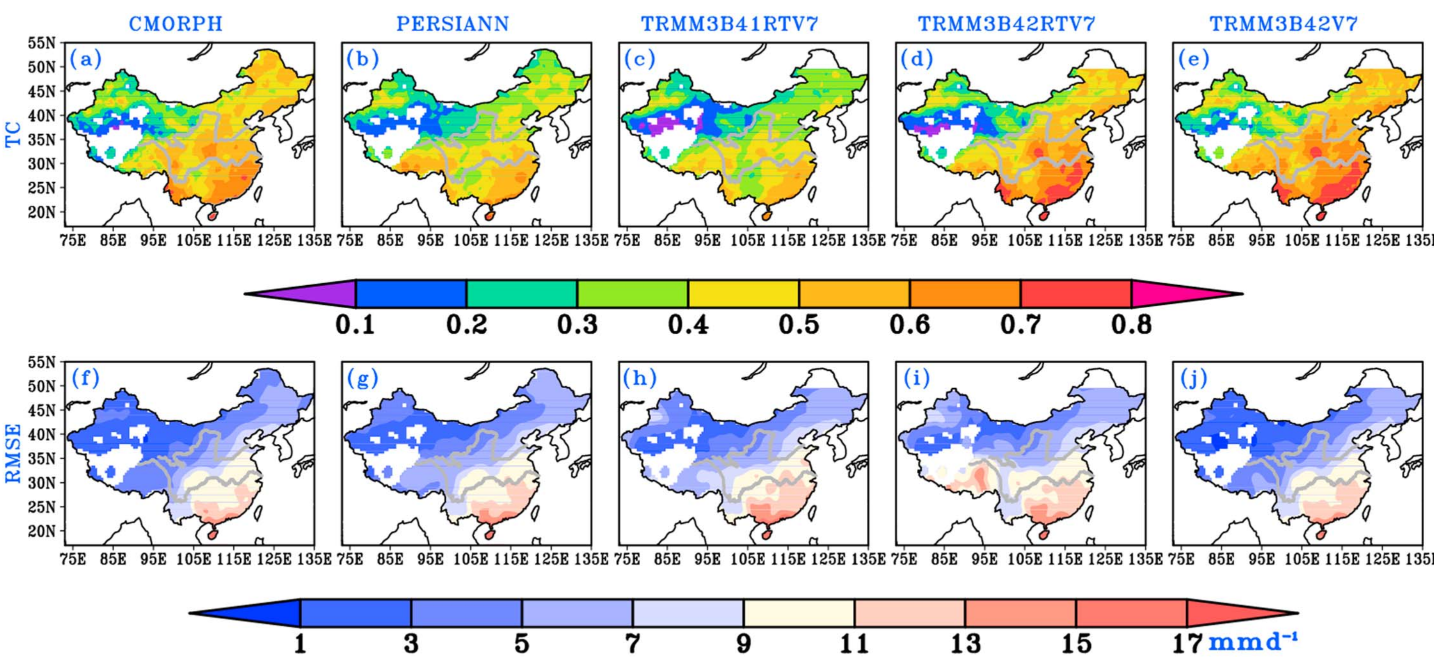

Figure A2. Spatial distribution of the TC and RMSE for each satellite precipitation product over 2000–2014.

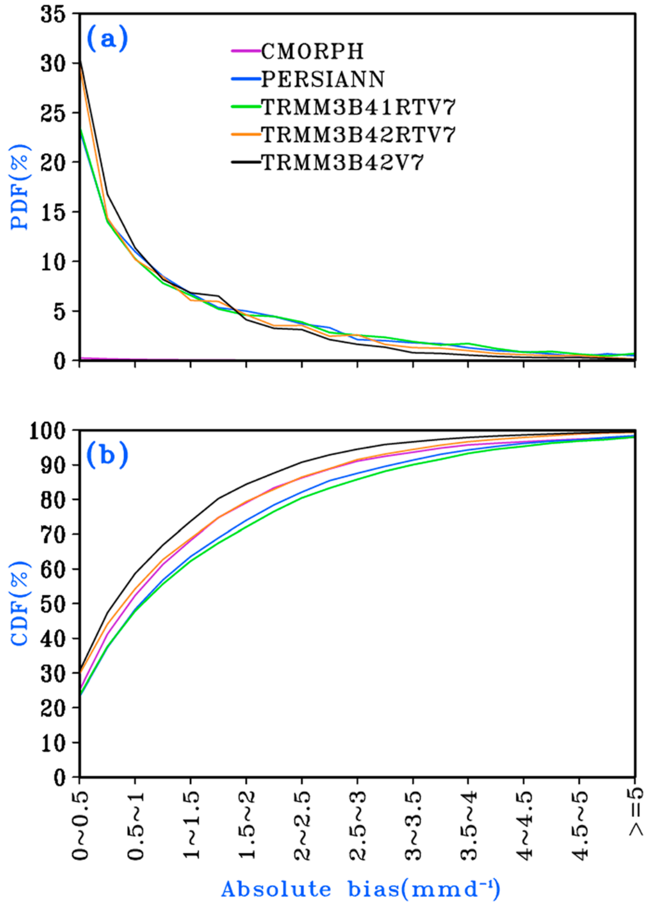

Figure A3. Probability distribution function (PDF) and cumulative distribution function (CDF) of the total error for each satellite precipitation product over China during 2000–2014.

TRMM3B42V7 data over western China, more ground gauge-based information over these regions should be taken into the bias adjustments. In addition, it is worth noting that the uncertainties in the TRMM3B42RTV7 and TRMM3B42V7 precipitation estimates are significantly reduced compared to the other three satellite products due to the adoption of the improved retrieval algorithms and more satellite data [*Yong et al.*, 2012; *Chen et al.*, 2013b; *Huffman and Bolvin*, 2013]. Moreover, the near-real-time product TRMM3B42RTV7 without bias adjustments tends to show the second best performance over most eastern China among the five satellite products. Given the fact that there are no bias adjustments included, the improvements in the TRMM3B42RTV7 over eastern China are encouraging and favorable for the operational applications. However, TRMM3B42RTV7 is still facing a great challenge to accurately detect the precipitation over the semiarid to arid regions in western China especially over Tibetan Plateau where the precipitation is largely overestimated. Therefore, it is necessary to develop much more sophisticated retrieval algorithms with the consideration of effects of terrain, ice/snow cover, surface properties, precipitation evaporation, etc. [*McCollum et al.*, 2000; *Grody and Weng*, 2008; *Yong et al.*, 2012; *Chen et al.*, 2013b; *Yang and Luo*, 2014] to improve the quality of precipitation estimates over these regions in the future.

Acknowledgments
This work was supported by the National Natural Science Foundation of China under grants 91537102 and 41175086 and the Jiangsu Collaborative Innovation Center for Climate Change. We are grateful to Center for Hydrometeorology and Remote Sensing (ftp://persiann.eng.uci.edu/pub/PERSIANN/tar_3hr/), NOAA climate prediction center (ftp://ftp.cpc.ncep.noaa.gov/precip/CMORPH_V1.0/RAW/0.25deg-3HLY), and NASA (ftp://disc2.nascom.nasa.gov/data/TRMM/Gridded) for allowing us to use the satellite precipitation data. We thank National Meteorological Information Center of the China Meteorological Administration for providing the gauge observed precipitation data. The authors acknowledge the Editor and three anonymous reviewers for the careful review and constructive comments.

Appendix A

Three additional figures are further given in this Appendix as follows: (1) TS for each satellite product in detecting the amplitude and pattern of variability of the seasonal and annual climatic mean precipitation over each subregion of China (Figure A1), (2) spatial distribution of the TC and RMSE for each satellite precipitation product during 2000–2014 (Figure A2), and (3) probability distribution function (PDF) and cumulative distribution function (CDF) of the total error for each satellite precipitation product over China during 2000–2014 (Figure A3).

References

Adler, R. F., et al. (2003), The version-2 global precipitation climatology project (GPCP) monthly precipitation analysis (1979–present), *J. Hydrometeorol.*, *4*, 1147–1167.

AghaKouchak, A., A. Behrangi, S. Sorooshian, K. Hsu, and E. Amitai (2011), Evaluation of satellite-retrieved extreme precipitation rates across the central United States, *J. Geophys. Res.*, *116*, D02115, doi:10.1029/2010JD014741.

AghaKouchak, A., A. Mehran, H. Norouzi, and A. Behrangi (2012), Systematic and random error components in satellite precipitation data sets, *Geophys. Res. Lett.*, *39*, L09406, doi:10.1029/2012GL051592.

Arkin, P. A., and B. N. Meisner (1987), The relationship between large-scale convective rainfall and cold cloud over the western hemisphere during 1982–84, *Mon. Weather Rev.*, *115*, 51–74.

Bartier, P. M., and C. P. Keller (1996), Multivariate interpolation to incorporate thematic surface data using inverse distance weighting (IDW), *Comput. Geosci.*, *22*(7), 795–799, doi:10.1016/0098-3004(96)00021-0.

Beighley, R. E., R. L. Ray, Y. He, H. Lee, L. Schaller, K. M. Andreadis, M. Durand, D. E. Alsdorf, and C. K. Shum (2011), Comparing satellite derived precipitation datasets using the Hillslope River Routing (HRR) model in the Congo River Basin, *Hydrol. Process.*, *25*, 3216–3229.

Bookhagen, B., and D. W. Burbank (2010), Toward a complete Himalayan hydrological budget: Spatiotemporal distribution of snow melt and rainfall and their impact on river discharge, *J. Geophys. Res.*, *115*, F03019, doi:10.1029/2009JF001426.

Bowman, K. P. (2005), Comparison of TRMM precipitation retrievals with rain gauge data from ocean buoys, *J. Clim.*, *18*, 178–190, doi:10.1175/JCLI3259.1.

Chen, C., Z. Yu, L. Li, and C. Yang (2011), Adaptability evaluation of TRMM satellite rainfall and its application in the Dongjiang River Basin, *Proc. Environ. Sci.*, *10*, 396–402.

Chen, S., et al. (2013b), Similarity and difference of the two successive V6 and V7 TRMM multisatellite precipitation analysis performance over China, *J. Geophys. Res. Atmos.*, *118*, 13,060–13,074, doi:10.1002/2013JD019964.

Chen, Y., E. E. Ebert, K. J. E. Walsh, and N. E. Davidson (2013a), Evaluation of TRMM 3B42 precipitation estimates of tropical cyclone rainfall using PACRAIN data, *J. Geophys. Res. Atmos.*, *118*, 2184–2196, doi:10.1002/jgrd.50250.

Chokngamwong, R., and L. S. Chiu (2008), Thailand daily rainfall and comparison with TRMM products, *J. Hydrometeorol.*, *9*(2), 256–266, doi:10.1175/2007JHM876.1.

Collischonn, B., W. Collischonn, and C. E. M. Tucci (2008), Daily hydrological modeling in the Amazon basin using TRMM rainfall estimates, *J. Hydrol.*, *360*, 207–216.

Dai, A., and C. Deser (1999), Diurnal and semi-diurnal variations in global surface wind and divergence fields, *J. Geophys. Res.*, *104*(D24), 31,109–31,125, doi:10.1029/1999JD900927.

Dai, A., X. Lin, and K. Hsu (2007), The frequency, intensity, and diurnal cycle of precipitation in surface and satellite observations over low- and mid-latitudes, *Clim. Dyn.*, *29*, 727–744, doi:10.1007/s00382-007-0260-y.

Ding, Y., and J. C. L. Chan (2005), The East Asian summer monsoon: An overview, *Meteorol. Atmos. Phys.*, *89*, 117–142.

Dinku, T., P. Ceccato, E. Grover-kopec, M. Lemma, S. J. Connor, and C. F. Ropelewski (2007), Validation of satellite rainfall products over East Africa's complex topography, *Int. J. Remote Sens.*, *28*(7), 1503–1526, doi:10.1080/01431160600954688.

Dinku, T., S. Chidzambwa, P. Ceccato, S. J. Connor, and C. F. Ropelewski (2008), Validation of high-resolution satellite rainfall products over complex terrain, *Int. J. Remote Sens.*, *29*(14), 4097–4110, doi:10.1080/01431160701772526.

Ebert, E. E., J. E. Janowiak, and C. Kidd (2007), Comparison of near-real-time precipitation estimates from satellite observations and numerical models, *Bull. Am. Meteorol. Soc.*, *88*, 47–64.

Faures, J. M., D. C. Goodrich, D. A. Woolhiser, and S. Sorooshian (1995), Impact of small-scale spatial rainfall variability on runoff modeling, *J. Hydrol.*, *173*, 309–326.

Fekete, B. M., C. J. Vörösmarty, J. O. Roads, and C. J. Willmott (2004), Uncertainties in precipitation and their impacts on runoff estimates, *J. Clim.*, *17*, 294–304.

Ferraro, R. R. (1997), Special sensor microwave imager derived global rainfall estimates for climatological applications, *J. Geophys. Res.*, *102*(D14), 16,715–16,735, doi:10.1029/97JD01210.

Ferraro, R. R., F. Weng, N. C. Grody, and L. Zhao (2000), Precipitation characteristics over land from the NOAA-15 AMSU sensor, *Geophys. Res. Lett.*, *27*, 2669–2672, doi:10.1029/2000GL011665.

Gao, X., Y. Xu, Z. Zhao, J. Pao, and F. Giorgi (2006), On the role of resolution and topography in the simulation of East Asia precipitation, *Theor. Appl. Climatol.*, *86*, 173–185.

Gebregiorgis, A. S., and F. Hossain (2013), Understanding the dependence of satellite rainfall uncertainty on topography and climate for hydrologic model simulation, *IEEE Trans. Geosci. Remote Sens.*, *51*, 704–718.

Giovannettone, J. P., and A. P. Barros (2009), Probing regional orographic controls of precipitation and cloudiness in the central Andes using satellite data, *J. Hydrometeorol.*, *10*, 167–182.

Gottschalck, J., J. Meng, M. Rodell, and P. Houser (2005), Analysis of multiple precipitation products and preliminary assessment of their impact on global land data assimilation system land surface states, *J. Hydrometeorol.*, *6*, 573–598.

Grimes, D. I. F., and M. Diop (2003), Satellite-based rainfall estimation for river flow forecasting in Africa. I: Rainfall estimates and hydrological forecasts, *Hydrol. Sci. J.*, *48*(4), 567–584.

Grody, N. C., and F. Weng (2008), Microwave emission and scattering from deserts: Theory compared with satellite measurements, *IEEE Trans. Geosci. Remote Sens.*, *46*(2), 361–375.

Gruber, A., and V. Levizzani (2008), Assessment of global precipitation products, a project of the World Climate Research Programme Global Energy and Water Cycle Experiment (GEWEX) radiation panel, *WCRP Report No. 128*, WMO/TD No. 1430, 50 pp.

Guo, H., S. Chen, A. Bao, J. Hu, B. Yang, and P. M. Stepanian (2016), Comprehensive evaluation of high-resolution satellite-based precipitation products over China, *Atmosphere*, *7*(1), 6, doi:10.3390/atmos7010006.

Habib, E., A. Henschke, and R. Adler (2009), Evaluation of TMPA satellite-based research and real-time rainfall estimates during six tropical related heavy rainfall events over Louisiana, USA, *Atmos. Res.*, *94*(3), 373–388.

Harris, A., S. Rahman, F. Hossain, L. Yarborough, A. C. Bagtzoglou, and G. Easson (2007), Satellite-based flood modeling using TRMM-based rainfall products, *Sensors*, *7*, 3416–3427.

Higgins, R. W., J. E. Janowiak, and Y. P. Yao (1996), A gridded hourly precipitation data base for the United States (1963–1993), *NCEP Clim. Predict. Cent. Atlas 1*, U.S. Dep. of Commer., NOAA, Camp Springs, Md.

Hirpa, F. A., M. Gebremichael, and T. Hopson (2010), Evaluation of high resolution satellite precipitation products over very complex terrain in Ethiopia, *J. Appl. Meteorol. Climatol.*, *49*(5), 1044–1051.

Hong, Y., K. L. Hsu, S. Sorooshian, and X. Gao (2005), Improved representation of diurnal variability of rainfall retrieved from the Tropical Rainfall Measurement Mission Microwave Imager adjusted Precipitation Estimation From Remotely Sensed Information Using Artificial Neural Networks (PERSIANN) system, *J. Geophys. Res.*, *110*, D06102, doi:10.1029/2004JD005301.

Hong, Y., R. F. Adler, F. Hossain, S. Curtis, and G. J. Huffman (2007a), A first approach to global runoff simulation using satellite rainfall estimation, *Water Resour. Res.*, *43*, W08502, doi:10.1029/2006WR005739.

Hong, Y., R. F. Adler, A. Negri, and G. J. Huffman (2007b), Flood and landslide applications of near real-time satellite rainfall products, *Nat. Hazards*, *43*(2), 285–294.

Hong, Y., D. Gochis, J. T. Cheng, K. L. Hsu, and S. Sorooshian (2007c), Evaluation of PERSIANN-CCS rainfall measurement using the NAME event rain gauge network, *J. Hydrometeorol.*, *8*, 469–482.

Hossain, F., and E. N. Anagnostou (2004), Assessment of current passive-microwave- and infrared-based satellite rainfall remote sensing for flood prediction, *J. Geophys. Res.*, *109*, D07102, doi:10.1029/2003JD003986.

Hou, A. Y., et al. (2014), The global precipitation measurement mission, *Bull. Am. Meteorol. Soc.*, *95*, 701–722, doi:10.1175/BAMS-D-13-00164.1.

Hsu, K., X. Gao, S. Sorooshian, and H. V. Gupta (1997), Precipitation estimation from remotely sensed information using artificial neural networks, *J. Appl. Meteorol.*, *36*, 1176–1190.

Huang, A., Y. Zhou, Y. Zhang, D. Huang, Y. Zhao, and H. Wu (2014), Changes of the annual precipitation over central Asia in the twenty-first century projected by multimodels of CMIP5, *J. Clim.*, *27*, 6627–6646.

Huffman, G. J., and D. T. Bolvin (2013), TRMM and other data precipitation data set documentation, Laboratory for Atmospheres, NASA Goddard Space Flight Center and Science Systems and Applications. [Available at ftp://precip.gsfc.nasa.gov/pub/trmmdocs/3B42_3B43_doc.pdf.]

Huffman, G. J., D. T. Bolvin, E. J. Nelkin, D. B. Wolff, R. F. Adler, G. Gu, Y. Hong, K. P. Bowman, and E. F. Stocker (2007), The TRMM multisatellite precipitation analysis (TMPA): Quasi-global, multiyear, combined-sensor precipitation estimates at fine scales, *J. Hydrometeorol.*, *8*(1), 38–55.

Hughes, D. A. (2006), Comparison of satellite rainfall data with observations from gauging station networks, *J. Hydrol.*, *327*, 399–410.

Janowiak, J. E., R. J. Joyce, and Y. Yarosh (2001), A real-time global half-hourly pixel-resolution infrared dataset and its applications, *Bull. Am. Meteorol. Soc.*, *82*, 205–217.

Janowiak, J. E., V. E. Kousky, and R. J. Joyce (2005), Diurnal cycle of precipitation determined from the CMORPH high spatial and temporal resolution global precipitation analyses, *J. Geophys. Res.*, *110*, D23105, doi:10.1029/2005JD006156.

Javanmard, S., A. Yatagai, M. I. Nodzu, J. BodaghJamali, and H. Kawamoto (2010), Comparing high-resolution gridded precipitation data with satellite rainfall estimates of TRMM_3B42 over Iran, *Adv. Geosci.*, *25*, 119–125, doi:10.5194/adgeo-25-119-2010.

Jiang, S., L. Ren, B. Yong, X. Yang, and L. Shi (2010), Evaluation of high-resolution satellite precipitation products with surface rain gauge observations from Laohahe Basin in northern China, *Water Sci. Eng.*, *3*(4), 405–417.

Joyce, R. J., J. E. Janowiak, P. A. Arkin, and P. Xie (2004), CMORPH: A method that produces global precipitation estimates from passive microwave and infrared data at high spatial and temporal resolution, *J. Hydrometeorol.*, *5*, 487–503.

Kan, M., A. Huang, Y. Zhao, Y. Zhou, B. Yang, and H. Wu (2015), Evaluation of the summer precipitation over China simulated by BCC_CSM model with different horizontal resolutions during the recent half century, *J. Geophys. Res. Atmos.*, *120*, 4657–4670, doi:10.1002/2015JD023131.

Kidd, C., V. Levizzani, J. Turk, and R. Ferraro (2009), Satellite precipitation measurements for water resource monitoring, *J. Amer. Water Resour. Assoc.*, *45*, 567–579.

Kidd, C., P. Bauer, J. Turk, G. J. Huffman, R. Joyce, K.-L. Hsu, and D. Braithwaite (2012), Intercomparison of high-resolution precipitation products over northwest Europe, *J. Hydrometeorol.*, *13*, 67–83.

Kidd, C. K., D. R. Kniveton, M. C. Todd, and T. J. Bellerby (2003), Satellite rainfall estimation using combined passive microwave and infrared algorithms, *J. Hydrometeorol.*, *4*, 1088–1104, doi:10.1175/1525-7541.

Kirstetter, P. E., Y. Hong, J. J. Gourley, M. Schwaller, W. Petersen, and J. Zhang (2013), Comparison of TRMM 2A25 products, version 6 and version 7, with NOAA/NSSL ground radar-based National Mosaic QPE, *J. Hydrometeorol.*, *14*, 661–669.

Kummerow, C., et al. (2000), The status of the Tropical Rainfall Measuring Mission (TRMM) after two years in orbit, *J. Appl. Meteorol.*, *39*(1), 1965–1982.

Kummerow, C., Y. Hong, W. S. Olson, S. Yang, R. F. Adler, J. McCollum, R. Ferraro, G. Petty, D.-B. Shin, and T. T. Wilheit (2001), The evolution of the Goddard Profiling Algorithm (GPROF) for rainfall estimation from passive microwave sensors, *J. Appl. Meteorol.*, *40*, 1801–1820.

Li, X. H., Q. Zhang, and C. Y. Xu (2012), Suitability of the TRMM satellite rainfalls in driving a distributed hydrological model for water balance computations in Xinjiang catchment, Poyang lake basin, *J. Hydrol.*, *426–427*, 28–38.

Li, X., Q. Zhang, and C. Xu (2014), Assessing the performance of satellite-based precipitation products and its dependence on topography over Poyang Lake basin, *Theor. Appl. Climatol.*, *115*, 713–729.

Li, Z., D. Yang, and Y. Hong (2013), Multi-scale evaluation of high-resolution multi-sensor blended global precipitation products over the Yangtze River, *J. Hydrol.*, *500*, 157–169.

Liechti, T. C., J. P. Matos, J. L. Boillat, and A. J. Schleiss (2012), Comparison and evaluation of satellite derived precipitation products for hydrological modeling of the Zambezi River Basin, *Hydrol. Earth Syst. Sci.*, *16*, 489–500.

Liu, J., A. Zhu, and Z. Duan (2012a), Evaluation of TRMM 3B42 precipitation product using rain gauge data in Meichuan watershed, Poyang lake basin, China, *J. Resour. Ecol.*, *3*(4), 359–366.

Liu, Z. (2015), Comparison of precipitation estimates between Version 7 3-hourly TRMM Multi-Satellite Precipitation Analysis (TMPA) near-real-time and research products, *Atmos. Res.*, *153*, 119–133.

Liu, Z. (2016), Comparison of Integrated Multisatellite Retrievals for GPM (IMERG) and TRMM Multisatellite Precipitation Analysis (TMPA) monthly precipitation products: Initial results, *J. Hydrometeorol.*, *17*(3), 777–790.

Liu, Z., D. Ostrenga, W. Teng, and S. Kempler (2012b), Tropical Rainfall Measuring Mission (TRMM) precipitation data and services for research and applications, *Bull. Am. Meteorol. Soc.*, *93*, 1317–1325, doi:10.1175/BAMS-D-11-00152.1.

McCollum, J. R., A. Gruber, and M. B. Ba (2000), Discrepancy between gauges and satellite estimates of rainfall in equatorial Africa, *J. Appl. Meteorol.*, *39*, 666–679.

Mehran, A., and A. AghaKouchak (2014), Capabilities of satellite precipitation datasets to estimate heavy precipitation rates at different temporal accumulations, *Hydrol. Process.*, *28*, 2262–2270.

Morrissey, M. L., J. A. Maliekal, J. S. Greene, and J. Wang (1995), The uncertainty of simple spatial averages using rain gauge networks, *Water Resour. Res.*, *31*(8), 2011–2017, doi:10.1029/95WR01232.

Nair, S., G. Srinivasan, and R. Nemani (2009), Evaluation of multi-satellite TRMM derived rainfall estimates over a Western State of India, *J. Meteorol. Soc. Jpn.*, *87*(6), 927–939.

Nasrollahi, N., K. Hsu, and S. Sorooshian (2013), An artificial neural network model to reduce false alarms in satellite precipitation products using MODIS and CloudSat observations, *J. Hydrometeorol.*, *14*, 1872–1883.

Nijssen, B., and D. P. Lettenmaier (2004), Effect of precipitation sampling error on simulated hydrological fluxes and states: Anticipating the Global Precipitation Measurement satellites, *J. Geophys. Res.*, *109*, D02103, doi:10.1029/2003JD003497.

Nykanen, D. K., E. Foufoula-Georgiou, and W. M. Lapenta (2001), Impact of small-scale rainfall variability on larger-scale spatial organization of land-atmosphere fluxes, *J. Hydrometeorol.*, *2*, 105–121.

Ochoa, A., L. Pineda, P. Crespo, and P. Willems (2014), Evaluation of TRMM 3B42 precipitation estimates and WRF retrospective precipitation simulation over the Pacific–Andean region of Ecuador and Peru, *Hydrol. Earth Syst. Sci.*, *18*, 3179–3193.

Qiao, L., Y. Hong, S. Chen, C. B. Zou, J. J. Gourley, and B. Yong (2014), Performance assessment of the successive Version 6 and Version 7 TMPA products over the climate-transitional zone in the southern Great Plains, USA, *J. Hydrol.*, *513*, 446–456.

Qin, Y., Z. Chen, Y. Shen, S. Zhang, and R. Shi (2014), Evaluation of satellite rainfall estimates over the Chinese Mainland, *Remote Sens.*, *6*, 11,649–11,672.

Rahman, S. H., D. Sengupta, and M. Ravichandran (2009), Variability of Indian summer monsoon rainfall in daily data from gauge and satellite, *J. Geophys. Res.*, *114*, D17113, doi:10.1029/2008JD011694.

Rozante, J. R., D. S. Moreira, L. G. G. de Goncalves, and D. A. Vila (2010), Combining TRMM and surface observations of precipitation: Technique and validation over South America, *Weather Forecasting*, *25*(3), 885–894.

Sapiano, M. R. P., and P. A. Arkin (2009), An intercomparison and validation of high-resolution satellite precipitation estimates with 3-hourly gauge data, *J. Hydrometeorol.*, *10*, 149–166.

Schulz, J., et al. (2009), Operational climate monitoring from space: The EUMETSAT Satellite Application Facility on Climate Monitoring (CM-SAF), *Atmos. Chem. Phys.*, *9*, 1687–1709.

Seo, K. H., J. Ok, J. H. Son, and D. H. Cha (2013), Assessing future changes in the East Asian summer monsoon using CMIP5 coupled models, *J. Clim.*, *26*(19), 7662–7675.

Serra, Y. L., and M. J. McPhaden (2003), Multiple time- and space-scale comparisons of atlas buoy rain gauge measurements with TRMM satellite precipitation measurements, *J. Appl. Meteorol.*, *42*, 1045–1059.

Shen, Y., A. Xiong, Y. Wang, and P. Xie (2010), Performance of high-resolution satellite precipitation products over China, *J. Geophys. Res.*, *115*, D02114, doi:10.1029/2009JD012097.

Sorooshian, S., K. Hsu, X. Gao, H. V. Gupta, B. Imam, and D. Braithwaite (2000), Evaluation of PERSIANN system satellite-based estimates of tropical rainfall, *Bull. Am. Meteorol. Soc.*, *81*, 2035–2046.

Sorooshian, S., X. Gao, K. Hsu, R. A. Maddox, Y. Hong, H. V. Gupta, and B. Iman (2002), Diurnal variability of tropical rainfall retrieved from combined GOES and TRMM satellite information, *J. Clim.*, *15*, 983–1001.

Sorooshian, S., R. Lawford, P. Try, W. Rossow, J. Roads, J. Polcher, G. Sommeria, and R. Schiffer (2005), Water and energy cycles: Investigating the links, *WMO Bull.*, *54*, 58–64.

Sorooshian, S., et al. (2011), Advancing the remote sensing of precipitation, *Bull. Am. Meteorol. Soc.*, *92*, 1271–1272.

Spencer, R. W. (1993), Global oceanic precipitation from the MSU during 1979–91 and comparisons to other climatologies, *J. Clim.*, *6*, 1301–1326.

Stisen, S., and I. Sandholt (2010), Evaluation of remote-sensing-based rainfall products through predictive capability in hydrological runoff modeling, *Hydrol. Processes*, *24*, 879–891.

Su, F., Y. Hong, and D. P. Lettenmaier (2008), Evaluation of TRMM Multisatellite Precipitation Analysis (TMPA) and its utility in hydrologic prediction in the La Plata Basin, *J. Hydrometeorol.*, *9*(4), 622–640.

Su, F., H. Gao, G. J. Huffman, and D. P. Lettenmaier (2011), Potential utility of the real-time TMPA-RT precipitation estimates in streamflow prediction, *J. Hydrometeorol.*, *12*, 444–455.

Susskind, J., P. Piraino, L. Rokke, L. Iredell, and A. Mehta (1997), Characteristics of the TOVS Pathfinder Path A dataset, *Bull. Am. Meteorol. Soc.*, *78*, 1449–1472.

Taylor, K. E. (2001), Summarizing multiple aspects of model performance in a single diagram, *J. Geophys. Res.*, *106*, 7183–7192, doi:10.1029/2000JD900719.

Tian, Y., C. D. Peters-Lidard, B. J. Choudhury, and M. Garcia (2007), Multitemporal analysis of TRMM-based satellite precipitation products for land data assimilation applications, *J. Hydrometeorol.*, *8*, 1165–1183.

Tian, Y., G. Huffman, R. Adler, L. Tang, M. Sapiano, V. Maggioni, and H. Wu (2013), Modeling errors in daily precipitation measurements: Additive or multiplicative?, *Geophys. Res. Lett.*, *40*, 2060–2065, doi:10.1002/grl.50320.

Turk, F. J., and S. D. Miller (2005), Toward improved characterization of remotely sensed precipitation regimes with MODIS/AMSR-E blended data techniques, *IEEE Trans. Geosci. Remote Sens.*, *43*, 1059–1069.

Turk, J. T., G. V. Mostovoy, and V. Anantharaj (2010), The NRL-blend high resolution precipitation product and its application to land surface hydrology, in *Satellite Rainfall Applications for Surface Hydrology*, edited by M. Gebremichael and F. Hossain, pp. 85–104, Springer, Dordrecht, Netherlands.

Vila, D., R. Ferraro, and R. Joyce (2007), Evaluation and improvement of AMSU precipitation retrievals, *J. Geophys. Res.*, *112*, D20119, doi:10.1029/2007JD008617.

Wang, T., S. Wong, and E. J. Fetzer (2015), Cloud regime evolution in the Indian monsoon intraseasonal oscillation: Connection to large-scale dynamical conditions and the atmospheric water budget, *Geophys. Res. Lett.*, *42*, 9465–9472, doi:10.1002/2015GL066353.

Wilheit, T. T., A. T. C. Chang, and L. S. Chiu (1991), Retrieval of monthly rainfall indices from microwave radiometric measurements using probability distribution functions, *J. Atmos. Oceanic Technol.*, *8*, 118–136.

Willmott, J. (1981), On the validation of model, *Phys. Geogr.*, *2*, 184–194.

Wu, L., and P. Zhai (2012), Validation of daily precipitation from two high-resolution satellite precipitation datasets over the Tibetan Plateau and the regions to its east, *Acta Meteorol. Sin.*, *26*(6), 735–745.

Xie, P., and P. A. Arkin (1998), Global monthly precipitation estimates from satellite-observed outgoing longwave radiation, *J. Clim.*, *11*, 137–164.

Xie, P., A. Chen, S. Yang, A. Yatagai, T. Hayasaka, Y. Fukushima, and C. Liu (2007), A gauge-based analysis of daily precipitation over East Asia, *J. Hydrometeorol.*, *8*, 607–626.

Xue, X., Y. Hong, A. S. Limaye, J. J. Gourley, G. J. Huffman, S. I. Khan, C. Dorji, and S. Chen (2013), Statistical and hydrological evaluation of TRMM-based Multi-satellite Precipitation Analysis over the Wangchu Basin of Bhutan: Are the latest satellite precipitation products 3B42V7 ready for use in ungauged basins?, *J. Hydrol.*, *499*, 91–99.

Yang, S., and E. A. Smith (2006), Mechanisms for diurnal variability of global tropical rainfall observed from TRMM, *J. Clim.*, *19*, 5190–5226.

Yang, Y., and Y. Luo (2014), Evaluating the performance of remote sensing precipitation products CMORPH, PERSIANN, and TMPA, in the arid region of northwest China, *Theor. Appl. Climatol.*, *118*, 429–445.

Yatagai, A., O. Arakawa, K. Kamiguchi, H. Kawamoto, M. I. Nodzu, and A. Hamada (2009), A 44-year daily gridded precipitation dataset for Asia based on a dense network of rain gauges, *SOLA*, *5*, 137–140.

Yong, B., L. L. Ren, Y. Hong, J. H. Wang, J. J. Gourley, S. H. Jiang, X. Chen, and W. Wang (2010), Hydrologic evaluation of Multisatellite Precipitation Analysis standard precipitation products in basins beyond its inclined latitude band: A case study in Laohahe basin, China, *Water Resour. Res.*, *46*, W07542, doi:10.1029/2009WR008965.

Yong, B., Y. Hong, L.-L. Ren, J. J. Gourley, G. J. Huffman, X. Chen, W. Wang, and S. I. Khan (2012), Assessment of evolving TRMM-based multisatellite real-time precipitation estimation methods and their impacts on hydrologic prediction in a high latitude basin, *J. Geophys. Res.*, *117*, D09108, doi:10.1029/2011JD017069.

10.1002/2016JD025456

Yong, B., L. Ren, Y. Hong, J. J. Gourley, Y. Tian, G. J. Huffman, X. Chen, W. Wang, and Y. Wen (2013), First evaluation of the climatological calibration algorithm in the real-time TMPA precipitation estimates over two basins at high and low latitudes, *Water Resour. Res.*, *49*, 2461–2472, doi:10.1002/wrcr.20246.

Yu, Z., H. Yu, P. Chen, C. Qian, and C. Yue (2009), Verification of tropical cyclone–related satellite precipitation estimates in mainland China, *J. Appl. Meteorol. Climatol.*, *48*, 2227–2241.

Zeng, H. W., L. J. Li, and J. Y. Li (2012), The evaluation of TRMM Multisatellite Precipitation Analysis (TMPA) in drought monitoring in the Lancang River Basin, *J. Geogr. Sci.*, *22*(2), 273–282.

Zhou, T., R. Yu, H. Chen, A. Dai, and Y. Pan (2008), Summer precipitation frequency, intensity, and diurnal cycle over China: A comparison of satellite data with rain gauge observations, *J. Clim.*, *21*, 3997–4010.